Published in final edited form as:
Nat Aging. 2022 March ; 2(3): 214–223. doi:10.1038/s43587-022-00181-4.

Cerebral amyloid angiopathy is associated with glymphatic transport reduction and time-delayed solute drainage along the neck arteries

Xinan Chen[1,#], **Xiaodan Liu**[2,#], **Sunil Koundal**[2], **Rena Elkin**[3], **Xiaoyue Zhu**[4], **Brittany Monte**[2], **Feng Xu**[4], **Feng Dai**[5], **Maysam Pedram**[2], **Hedok Lee**[2], **Jonathan Kipnis**[6], **Allen Tannenbaum**[1,7,+], **William E. Van Nostrand**[4,+], **Helene Benveniste**[2,8,+,*]

[1] Department of Applied Mathematics and Statistics, Stony Brook University, Stony Brook, NY, USA

[2] Department of Anesthesiology, Yale School of Medicine, New Haven, CT, USA

[3] Department of Medical Physics, Memorial Sloan Kettering Cancer Center, New York City, NY, USA

[4] George and Anne Ryan Institute for Neuroscience and the Department of Biomedical and Pharmaceutical Sciences, University of Rhode Island, RI, USA

[5] Yale Center for Analytical Sciences, Yale School of Public Health, New Haven, CT

[6] Center for Brain Immunology and Glia (BIG), Department of Pathology and Immunology, Washington University, St. Louis, MO, USA.

[7] Department of Computer Science, Stony Brook University, Stony Brook, NY, USA

[8] Department of Biomedical Engineering, Yale School of Medicine New Haven, CT, USA

Cerebral amyloid angiopathy (CAA) is a common disease in older adults that contributes to dementia[1–3]. In CAA, amyloid beta (Aβ) is deposited along either capillaries (Type 1) or vessel walls (Type 2)[4], with the underlying pathophysiology incompletely understood[5]. Here, we developed novel imaging and analysis tools based on regularized Optimal Mass Transport (rOMT) theory[6,7] to characterize cerebrospinal fluid (CSF) flow dynamics and glymphatic transport in a transgenic CAA type 1 rat model. We discovered that in CAA,

---

[*] Corresponding author: Helene Benveniste, MD, PhD, Department of Anesthesiology, Yale School of Medicine, New Haven, CT, USA, helene.benveniste@yale.edu, Telephone: 203-737-1516 (office); 631-275-1685 (cell).

[#] These authors contributed equally.

[+] These authors jointly supervised this work.

Author contributions

X.C, R.E and A.T. designed all the computational fluid dynamics algorithms based on regularized optimal mass transport, performed all the rOMT analysis of the data and wrote the rOMT supplemental method section. X.L. and S.K. performed all of the brain glymphatic MRI experiments and morphometric analysis of the brain data. S.K. and H.B. designed, performed, and analyzed all MRI experiments of the lymph node drainage. X.Z, B.M. and F.X. performed immunohistochemistry and assisted with blinded data analysis and quantifications. F.D. assisted with statistical design and data analysis. M.P. assisted with analysis of LN time activity data. H.L. assisted in the quantitative MRI data analysis and helped design and perform initial glymphatic whole brain experiments. J.K. provided intellectual contribution and interpretation of the lymph node data and participated in manuscript writing. A.T. designed the mathematical rOMT framework, provided intellectual contribution, oversaw rOMT data analysis, and contributed to writing the manuscript. W.VN. designed the biological components of the experiments with H.B., created the rTg-DI rat model and supplied this strain and WT littermates for the study; provided intellectual contributions and participated in manuscript writing. H.B designed all the experiments, oversaw data analysis and interpretation, and wrote the manuscript.

CSF move more rapidly along the peri-arterial spaces that serve as influx routes to the glymphatic system. The observation of high-speed CSF flow currents in CAA was unexpected given the build-up of microvascular Aβ. However, the velocity flux vector analysis revealed that the CSF currents in CAA was partly diverted away from the brain, resulting in overall decreased glymphatic transport. Imaging at the neck showed that drainage to the deep cervical lymph nodes occurred along the carotid arteries and was time-delayed in CAA implying that upstream connections to the meningeal lymphatics were altered. Based on our findings we propose that in CAA, glymphatic transport as well as lymphatic drainage are compromised and that both systems represent therapeutic targets for treatment of CAA-related cognitive decline and dementia.

The discovery of the glymphatic system and meningeal lymphatics has led to new hypotheses of waste clearance processes for sustaining cognitive health throughout the given lifespan and for establishing central nervous system (CNS) immune surveillance[8,9]. Glymphatic and lymphatic system function decreases with aging[10,11] as well as with Alzheimer's disease (AD)[12,13], cerebral small vessel disease[7], and Parkinson's disease[14]. Remarkably, glymphatic system function and drainage to the cervical lymph nodes have not yet been explored in CAA. CAA belongs to the class of amyloidal cerebral small vessel diseases that includes sporadic and familial forms[15,16]. Clinically, CAA is a leading cause of brain hemorrhage and is strongly associated with vascular cognitive impairment and dementia[15,17]. The underlying pathophysiology of CAA remains incompletely understood. One hypothesis poses that waste, including Aβ, drains from the brain along the walls of arteries; and this pathway, also known as *intramural arterial drainage* (IPAD)[18,19], become compromised with aging thereby causing CAA. The IPAD hypothesis is in direct opposition to the current glymphatic system model where waste drainage[20] occurs along small cerebral veins that merge into larger neck veins before entering the lymphatic system[21].

To address the knowledge gap of glymphatic system function implicated with CAA, we analyzed CSF flow dynamics in relation to glymphatic transport, as well as drainage to the cervical lymph nodes in both healthy and CAA brains by combining dynamic contrast enhanced MRI (DCE-MRI), and computational fluid dynamics (CFD) based on regularized rOMT[6,7]. Specifically, we used the CAA type 1 transgenic rat (rTg-DI) line, which expresses human Swedish/Dutch/Iowa vasculotropic mutant amyloid-beta precursor protein (AβPP), and cause Aβ deposition along the capillaries. The progressive accumulation of CAA pathology in rTg-DI rats is robust and well-documented[22–24]. In 12 month (M) old rTg-DI rats 50–70% of capillaries in the cortex, hippocampus and thalamus are covered with fibrillar Aβ and associated with a strong neuroinflammatory response (Extended Data Figs. 1 and 2)[22,24]. We utilized intrathecal gadoteric acid (Gd-DOTA) with DCE-MRI for measurement of CSF flow and glymphatic transport in separate cohorts of 3M, 6M and 12M old heterozygous rTg-DI rats and wild-type (WT) littermate controls. The DCE-MRI data was processed by our novel computational analytical framework based on rOMT theory (Supplementary Methods and Supplementary Information Figs. 1–4)[6,7]. The rOMT model incorporates advection (bulk-flow) and diffusion terms to calculate solute and fluid transport within the brain[7]. Specifically, the rOMT framework derives trajectories of fluid and solute movement – known as 'pathlines' - over a finite tracer circulation time[7] (Supplementary Information Figs. 2a–c). By combining the rOMT analysis with quantitative morphometry, speed maps of solute and fluid transport in the CSF and tissue compartment (glymphatic system) can be separately computed (Supplementary Information Figs. 2d–f). The speed maps capture two scalar measurements of the transport: (1) volume flux (*v-flux*) = volume of the pathlines representing the total solute transport over a ~2h time-frame, and (2) *speed* = mean solute speed within the pathline network. For example, the *v-flux* of the tissue compartment represents the volume of glymphatic transport, and the tissue speed map visualizes solute speed within the glymphatic system. In addition, rOMT derives the ***velocity flux vectors*** of the solute streams, and the velocity flux vector magnitude indicates the distance a given particle has travelled, while the velocity phase shows direction. The rOMT analysis also provides information about the transport modes (i.e., diffusion vs. advection) via the computation of the Péclet number along the pathlines. The Péclet (*Pe*) number is a standard scalar dimensionless quantity describing the ratio of the rate of advection versus that of diffusion. We also derived *Pe* maps (Supplementary Information Fig. 2b) which at the local level show the relative tendency of advection or diffusion-dominated motion of the solute.

We first characterized solute speed within the CSF compartment and glymphatic system across WT and rTg-DI rats. Notably, the CSF compartment as defined in this study includes the large perivascular spaces (PVS) along the pial surface arteries, but *not* PVS of the brain parenchyma. Population-averaged CSF speed maps of the 12M cohorts of WT (N=8) and rTg-DI (N=10) rats are shown in Figs. 1a–d. Compared to WT rats, solute speed in the rTg-DI rats was more rapid throughout the CSF compartment, in particular along the PVS of the circle of Willis and middle cerebral arteries, which serves as major influx routes to the glymphatic system (Fig. 1b). Corresponding statistical parametric maps (color coded for p-values) documented higher solute speed in rTg-DI rats throughout the CSF compartment in comparison to WT rats (Fig. 1e, f). We also implemented morphometric analysis by acquiring anatomical brain scans of each rat (Extended data Fig. 3) and analysis of the mean solute *speed* of the CSF compartment between groups was controlled for with CSF volume as a covariance factor. In the WT cohorts, the mean CSF solute *speed* was unchanged across ages (Fig. 1g). However, in rTg-DI rats the mean CSF solute *speed* increased significantly by ~30% from 6M to 12M (p-value < 0.0001, Fig. 1g), and CSF solute *speed* of 12M rTg-DI rats was ~20% higher compared to 12M WT rats (p-value = 0.003, Fig. 1g). The brain-wide glymphatic mean solute *speed* between groups revealed no changes at any age (Fig. 1h). However, the corresponding voxel-wide statistical parametric mapping analysis revealed multiple focal areas scattered throughout the forebrain with significantly higher speed in WT compared to rTg-DI rats (Figs. 1i, j). Extended data Fig. 4 shows the regional distribution of glymphatic speed differences across the two strains in the 12M cohorts in more anatomical detail.

Analysis of glymphatic *v-flux* across groups was performed with tissue compartment volume as a covariate factor. In WT rats, the mean glymphatic *v-flux* significantly increased by ~15% from 3M to the 12M (p-value =0.037, Fig. 1k). Further, a ~20% decrease of the mean glymphatic *v-flux* was documented in 12M rTg-DI rats compared to age-matched WT rats (p-value =0.017, Fig. 1k). Regional analysis showed that in the hippocampus where CAA pathology is extensive in rTg-DI rats[22,24], glymphatic *v-flux* was decreased compared to 12M WT (Fig. 1l). On the other hand, in the cerebellum where CAA pathology is absent, glymphatic *v-flux* was similar between the WT and rTg-DI groups at any age (Fig. 1m). Analysis of *v-flux* within the CSF compartment revealed no changes between the two groups at any age (p-value > 0.05). Several studies have shown that increased cardiovascular pulsatility drives CSF flow and glymphatic transport[25,26] and we observed a significant decline in heart rate with age for both groups (Extended Data Fig. 5). Furthermore, a slight ~10% decrease in the mean heart rate was observed for 12M rTg-DI rats compared to 12M WT (Extended Data Fig. 5).

To further understand the relationship between high-speed CSF flow and reduced glymphatic transport in rTg-DI rats, we implemented velocity flux vectors analysis. Figs. 2a and 2b show the spatial distribution of velocity flux vectors (color coded for magnitude) from a 12M WT rat overlaid on the corresponding CSF mask. From this data in normal brain, we made the following observations: 1) velocity flux vectors originate in the basal cistern and point towards the tissue bed (Fig. 2a); 2) the velocity flux vectors have lower magnitude (blue arrows) within the tissue bed; 3) at the level of the circle of Willis (Fig. 2b, white box), the velocity flux vectors are configured in bilateral symmetry about the midline; 4) in the olfactory fossa (Fig. 2a, black box) high magnitude streams (red arrows) with direction towards the olfactory bulb were noted. The corresponding vector data from a 12M rTg-DI rats are shown in Figs. 2c, d and revealed a remarkably different pattern. First, a dense cluster of high magnitude vectors (red arrows) with direction towards the olfactory fossa was noted (Fig. 2c). Second, very few low-magnitude arrows were present within the tissue bed. Third, at the circle of Willis, (Fig. 2d, white box) the high-speed streams were partly directed away from the brain. From these data, we concluded that in 12M rTg-DI rats the high-speed, redirected CSF streams were linked to the reduction of glymphatic transport.

The high magnitude velocity flux vectors along the skull base exhibited a clear directional trend implying advective transport. To test this assumption, we calculated the Péclet numbers of the WT and rTg-DI cohorts. In the WT rat, the CSF-rich areas were characterized by advective transport (higher *Pe* numbers) while pathlines in the tissue were associated by lower *Pe* numbers, thus implying diffusive transport (Figs. 2e, f). In the rTg-DI rat, advective solute transport was noted throughout the CSF compartment, as well as in the cerebellum, and olfactory fossa (Fig. 2g, h). The statistical analysis of the *Pe* data revealed that the mean CSF *Péclet* number of rTg-DI rats increased by ~34% from 6M to 12M, p-value < 0.0001 (Fig. 2i). Further, the mean CSF *Péclet* of 12M rTg-DI rats was ~33% higher compared to 12M WT rats (Fig. 2i). There were no differences in the mean tissue *Péclet* number across age or strains (Fig. 2j).

The advective, redirected CSF flow at the skull base and glymphatic *v-flux* reduction observed in CAA is likely associated with the buildup of microvascular Aβ and perivascular neuroinflammation. Alternatively, glymphatic *v-flux* reduction may also be associated with altered AQP4 water channel expression on the glial end-feet. Indeed, studies have shown that the peri-vascular AQP4 expression pattern is altered in several neurodegenerative disease states including aging[10], cerebral small vessel disease[7] and AD[27]. In WT rats, the peri-vascular AQP4 expression pattern in the ventral hippocampus was unchanged from 3M to 12M (Extended Data Figs. 6a–c). In contrast, in rTg-DI rats the AQP4 peri-vascular expression weakened at 6M and 12M compared to 3M (Extended Data Fig. 6d–f). We quantified the peri-vascular AQP4 expression of the groups using the polarization index method[7]. There were no differences between strains at 3M (Extended Data Fig. 6g), however, at 6M and 12M statistically significant decreases in the AQP4 polarization index were documented in rTg-DI compared to WT rats (Extended Data Figs. 6h, i).

To explore waste clearance in CAA, we developed another DCE-MRI approach to dynamically map drainage pathways from the CNS to the cervical lymph nodes. For this purpose, we used a 2-cm radiofrequency (RF) surface coil positioned above the neck of the anesthetized rat in supine position (Fig. 3a). With the RF coil in this position the neck vasculature and cervical lymph nodes are within the field of view (Figs. 3b). Second, we used the Gd-based tracer GadoSpin-P (molecular weight 200 kDa) that enters more slowly into the glymphatic system compared to the smaller molecular weight tracers[28], but provides ideal conditions for visualizing the major drainage streams on the neck to the dcLN. Anatomically, the cervical lymph nodes were easily identifiable on the post-contrast T1-weighted MRIs (Figs. 3c, d). The superficial cervical lymph nodes included the laterally positioned parotid lymph nodes and 2–3 submandibular lymph nodes (Figs. 3c, d). The deep cervical lymph nodes (dcLNs) were most often positioned immediately lateral to the common carotid artery bifurcation (Figs. 3c). A representative image of a dcLN from a normal, ~3M Sprague Dawley (SD) rat is shown in Fig. 3d. The corresponding drainage maps (represented by the signal intensity time averaged over ~2h normalized to the CSF signal) reveal higher signal intensity in the hilum where the efferent lymphatic vessel exits the lymph node (Figs. 3e). Representative dynamic time signal curves (TSCs) extracted from a right- and left dcLN of a normal rat are shown in Fig. 3f and demonstrate that 1) tracer uptake steadily increased and peaked at ~70 min from the time of GadoSpin-P administration into CSF, and 2) the right and left dcLN appear to drain equally well. Extended Data Fig. 7a shows a larger series of TSCs extracted from dcLN of normal rats (N=6, number of dcLN = 11), revealing that the signal peaks at ~80 min. The corresponding TSCs from the parotid lymph nodes revealed a slower drainage pattern compared to the dcLN (Extended Data Fig. 7b). Finally, TSCs from the submandibular lymph nodes demonstrated no drainage of GadoSpin-P (Extended Data Fig. 7c). Next, we looked at the 3D maps of the entire neck region to identify the main anatomical routes of solute drainage to the dcLN in normal rats. Fig. 3g shows a representative 3D signal map demonstrating drainage streams along the internal carotid artery (ICA), external carotid artery (ECA), and their branches, including the facial artery. The ECA associated streams seemed to coalesce with the dcLN (Fig. 3h). Importantly, the streams along the carotid arteries appeared ‘distinct’ and were not encircling the vasculature, suggesting that draining occurred within well-defined channels. This drainage pattern was robustly expressed across all the rats. To explore the directionality of the signal streams in relation to the dcLNs, we derived the corresponding velocity flux vectors. Figs. 3i shows high magnitude velocity flux vectors along the ECA pointed towards the right dcLN from a normal rat. This directional pattern of the vectors along the ECA towards the dcLN was observed in the majority of the normal rats (Extended Data Fig. 7d–f). The velocity flux vectors along the ICA and efferent lymphatics (when visible) were typically of lower magnitude and the directions more random. From these data we concluded that 1) in normal rats, solute drainage from the CNS to the dcLN involved discrete conduits along the neck arteries, and 2) solutes from the CNS drained primarily to the dcLN and to a lesser degree to the parotid lymph nodes. We then investigated drainage to the cervical lymph nodes in 9–10 M WT (N=4) and age-matched rTg-DI (N=4) rats with severe CAA. Anatomical and corresponding signal maps of the dcLN showed that the drainage pattern in the WT (Figs. 4a, b) was similar to that of the rTg-DI rat (Figs. 4c, d). Further, the signal maps associated with the neck arteries demonstrated drainage to the dcLN along the ICA and ECA in both WT (Fig. 4e) and rTg-DI (Fig 4f) rats. Notably, the TCS from the dcLN of rTg-DI rats (Fig. 4h) were right-shifted compared to those of the WT rats (Fig. 4g) indicating time-delayed drainage from CNS to the dcLN in CAA. Indeed, for the left dcLN of rTg-DI rats the time-to-peak was delayed by ~25 min when compared to the WT rats (WT (N=4) Left dcLN peak time: 65.8min ± 5.8 min vs rTg-DI (N=4) dcLN peak time 91.0 ± 7.0 min, mean difference = 25.2 min, 95% CI = [2.8, 47.6] min, p-value =0.017). A similar time-to-peak delay was observed for the right dcLN of the rTg-DI rats: (WT (N=4) Right dcLN peak time: 65.9 min ± 5.8 min vs rTg-DI (N=4) dcLN peak time 93.8 ± 5.7 min, mean difference = 28.0 min, 95% CI = [8.0, 47.9] min, p-value =0.007). The TSCs extracted from the parotid lymph nodes showed that in the rTg-DI rats, GadoSpin-P drainage ‘spilled over’ to the parotid lymph nodes (Fig. 4j) but not in WT rats (Fig. 4i), possibly implying rerouting of waste drainage pathways from the CNS in CAA. Drainage to the submandibular lymph nodes was at noise level for both WT and rTg-DI rats (results not shown). We also analyzed the directional pattern of the velocity flux vectors associated with the neck arteries and dcLN of the rTg-DI and WT rats. Fig. 4k shows the velocity flux vectors along the carotid arteries and dcLN from a WT rat demonstrating a similar direction of solute streams along the ECA towards the dcLN as observed in the normal, younger SD rats (Extended Data Fig. 7). Streaming along the ECA towards the dcLN was also observed in the rTg-DI rat (Fig. 4l). From these data, we concluded that compared to WT rats, solute drainage to the dcLN in rTg-DI rats with severe CAA type 1 was time-delayed, and with ‘spill-over’ drainage to the parotid lymph nodes.

Discussion

CAA is a common pathology in older adults and often co-occurs with AD[29,30]. Here, we documented that CSF and solute influx along the PVS of the large cerebral arteries, was more rapid and strongly advective in rats with severe CAA type 1. Furthermore, in CAA a fraction of the CSF flow currents bypassed the brain, resulting in decreased glymphatic transport and slower than normal drainage to the cervical lymph nodes. It is plausible that the altered CSF flow dynamics in CAA reflects blocked passage via the glymphatic system due to microvascular Aβ deposits[22]. The glymphatic transport reduction observed in CAA is in range with that reported in spontaneously hypertensive stroke prone (SHRSP) rats in which the brain-wide glymphatic transport was reduced by ~15%[7]. Intriguingly, although SHRSP and CAA rats are both associated with global reductions in glymphatic transport, their corresponding CSF flow profiles diverge. In SHRSP rats, CSF flow at the skull base was observed to be ‘sluggish’ secondary to PVS remodeling and vascular stiffness[31–33] while it is hyperdynamic in CAA. As the rTg-DI rats do not develop hypertension the more rapid CSF flow and reduced glymphatic transport is likely caused by the capillary Aβ deposition and extensive neuroinflammation[24]. Notably, in the rTg-DI transgenic rat model, Aβ is produced in the neurons only, and moves towards the capillaries for attempted transport across the blood brain barrier (BBB)[34,35]. It generally assumed that the deposition of Aβ occurs because the familial Dutch and Iowa CAA mutations interfere with the low-density lipoprotein receptor-related protein (LRP)/Aβ interactions and cannot be transported across the BBB and instead assemble into fibrils[34]. Other factors to consider in interpretation of our data in CAA include choice of anesthesia, body position and circadian rhythm which can all influence glymphatic transport[36–39]. However, anesthesia and supine positioning was identical across all groups, and the rats were scanned during their light cycle in a counter balanced manner and these factors are unlikely to have influenced the differences between groups.

Our study also revealed weakened peri-vascular AQP4 polarization in rTg-DI compared to WT rats. AQP4 water channel expression is known to change in neurodegenerative states including in aging with neuroinflammation[10]. In CAA rTg-DI rats, the excessive neuroinflammation might have contributed to the reduction in peri-vascular AQP4 polarization. A recent paper by Wang et al.,[40] documented that astrocytic endfoot size correlates with cerebral vessel diameter. Hence, in CAA where Aβ deposition and associated neuroinflammation influence the capillaries, it could be hypothesized that the endfeet change and thereby affect the overall AQP4 expression pattern. However, astrocytic endfeet are dynamic structures with active transport targets, including cytoskeletal rearrangements in which those factors may also influence the AQP4 relocation process in CAA; thus, studies are needed for better understanding of these processes.

Examination of solute drainage to the cervical lymph nodes revealed distinct signal streams along the large neck arteries in both WT and rTg-DI rats in agreement with earlier reports from normal rats[41]. The drainage conduits on the anterior surface of the carotid arteries are likely authentic lymphatics connecting to afferent lymphatics that drain to the dcLN, similar to what has been reported along the aorta in the mouse[42]. Future studies will be needed to determine the exact anatomy of the conduits in the rat. Discovery of solute drainage along the neck arteries was unexpected, given that the glymphatic system model stipulates peri-venous drainage merging to the neck veins → lymph[21]. In humans, the majority of the dcLNs are situated near the large neck veins and not arteries[43], thus the finding of drainage along the neck arteries may be unique to the rat. Indeed, in the rat, the internal jugular vein is missing[44], and venous drainage occurs via the larger external jugular vein[45]. Our observation of drainage along the neck arteries including the ECA does not directly support the IPAD model that waste drains in a ‘retrograde’ manner from the brain along the walls of the cortical penetrating arteries including the leptomeningeal arteries[18,46]. The most plausible explanation for solute streams observed along the ECA are upstream connections to meningeal lymphatics including those along the middle meningeal artery which branches from the ECA[47,48]. Further, we also speculate that the drainage lag time observed in CAA reflects the slower transit of solutes through the glymphatic system due to the build-up of Aβ. Alternatively, given the rerouting of CSF towards the olfactory fossa in rTg-DI rats, it is also plausible that the time delay implies altered egress pathways. In other words, drainage from the olfactory fossa would involve the cribriform plate → nasal cavity and the travel distance to the dcLN would therefore be longer than from the skull-base[49].

In summary, our results show that in CAA glymphatic transport as well as lymphatic drainage are compromised and therefore both systems represent therapeutic targets for treatment of CAA-related cognitive decline and dementia. More investigations of other types of CAA including CAA type 2 and mixed dementias are needed to fully understand the mechanisms underlying waste disposal in humans.

Methods

Rat strains and housing

Female hemizygous rTg-DI CAA type 1 rat line (Sprague Dawley (SD) background), which expresses human Swedish/Dutch/Iowa vasculotropic mutant amyloid-beta precursor protein (AβPP) under control of the neuronal Thy1.2 promoter and produces chimeric Dutch/Iowa CAA mutant Aβ peptides in brain were bred and maintained at the University of Rhode Island (URI). Unless stated otherwise, separate cohorts of the in-house bred rTg-DI female rats and non-transgenic female littermates (serving as WT controls) were used at 3-months (M), 6M and 12M of age. Sample size the different age cohort are listed in main text of the result section. The rats were transported from URI to Yale University at least 4–6 weeks prior to scheduled MRI imaging. A separate series of 4-month-old SD female rats were purchased from Charles River (Charles River Laboratories International, Inc., NC, USA) for the initial characterization of cervical lymph node drainage experiments. Separate groups of 9–10M female WT and 9–10M female rTg-DI rats were used for MRI experiments of cervical lymph node drainage and sample size and age ranges of the different cohort are listed in main text of the result section. All rats were housed in an environment with controlled temperature, individually ventilated cages, and humidity, 12/12 h light cycle from 7:00 A.M to 7:00 P.M and fed standard chow and water *ad libitum*. All the animal work was approved by the local institutional animal care and use committees at URI, Rhode Island, USA and Yale University, New Haven, USA.

Anesthesia and surgery for animals before and during MRI scans

All rats underwent anesthesia and experimentation during their light cycle in a counter-balanced manner across strains. The rats induced with 3% isoflurane delivered into an induction chamber in 100% oxygen and then given dexmedetomidine (0.01mg/kg i.p.) mixed with glycopyrrolate (0.02 mg/kg i.p.). The rats were allowed to breathe spontaneously, and the body temperature was strictly controlled at around 37°C using a heating pad. Anesthesia for surgery was maintained with isoflurane (2–2.5%). The anesthetized rats were placed in a stereotaxic frame and a small 5-mm copper tube (0.32 mm o.d., Nippon Tockushukan, MFG. CO., LTD, Tokyo, Japan) attached to a PE 10 microcatheter was positioned into the CSF compartment via the cisterna magna (CM) and secured in place using cyanoacrylate glue. After surgery, the rats were transferred to the MRI animal bed equipped with a heating water-bed and breathing nose cone.

MRI acquisitions

All MRI acquisitions were performed on a Bruker 9.4T/16 magnet (Bruker BioSpin, Billerica MA, USA) interfaced to an Avance III console controlled by Paravision 6.0 software. The rats were all imaged in the supine position. Anesthesia during MRI was maintained with a subcutaneous infusion of dexmedetomidine (~0.009 mg/kg/hr) supplemented with low-dose, ~1% isoflurane delivered via a nose cone in a 1:1 Air:O_2 mixture[36]. Heart rate (HR) via oxygen saturation monitoring and body temperature were continuously monitored by an MRI-compatible non-invasive monitoring system (SA Instruments, Stony Brook, NY, USA). The body temperature was kept within a range of 36.5 to 37.5°C using a heated waterbed and oxygen saturation was kept ≥ 97% during the MRI experiments.

Whole brain MRI

A 30-mm ID planar surface radiofrequency (RF) coil (Bruker BioSpin, Billerica, MA, USA) was placed under the head of the rats for RF signal reception and a custom-made volume transmit RF coil designed with an internal diameter of 50 mm was used as RF signal transmitter. A reference phantom filled with 0.1 mM Gd-DOTA was placed in the field of view (FOV) for the signal intensity normalization between the frames. MRI imaging included: (1) 3D-Proton density weighted (PDW) images (for anatomical segmentation and morphometry); (2) Pre-contrast (baseline) T1-weighted images; and (3) post-contrast T1-weighted imaging. A single flip angle spoiled gradient echo (SPGR) sequence was used to acquire 3D PDW MRIs: (repetition time (TR) = 50ms, echo time (TE) = 4ms, flip angle (FA) = 7°, Average = 1, field of view (FOV) = 30×30×15mm, spatial resolution = 0.234×0.234×0.234mm, scan time = 6 mins 50s.

Dynamic contrast enhanced whole brain MRI: For measuring the glymphatic transport, a set of 3D T1 weighted scans were acquired dynamically before and after contrast administration using a single flip angle spoiled gradient echo (SPGR) sequence: TR=15ms, TE=4ms, FA=15°, Average = 2, FOV = 32×30×30mm, the spatial resolution= 0.302×0.300×0.300mm, acquisition time/scan = 5mins). After three baseline T1-weighted scans, 30 μL of 1:37 gadoteric acid (Gd-DOTA, DOTAREM, Guerbert LLC, Carol Stream IL) diluted in sterile water was infused at a rate of 1.5 μL/min into CSF through the CM catheter using an infusion pump for a total of 20 min. Post-contrast T1-weighted scans continued for a total 160 min. The effect of cisterna magna infusion of contrast tracers only transiently and minimally perturbs the intracranial pressure in rodents and previously reviewed in detail by Benveniste et al.,[50] and we refer interested readers to this recent overview for more information.

DCE-MRI of lymph nodes on the neck: A 2 cm planar surface receive radiofrequency (RF) coil (Bruker BioSpin, Billerica, MA, USA) was placed above the neck of the rat in supine position (Fig. 3a) with the same volume RF transmit coil (50-mm i.d.) used for the whole brain DCE-MRI studies[51]. With this coil part of the brain, spine and cervical lymph nodes were included within the FOV. A set of 3D T1 weighted scans were acquired dynamically before and after contrast administration using a single flip angle SPGR sequence: TR=15ms, TE=4ms, FA=15°, Average = 1, FOV = 30×30×30mm, Matrix = 150×150×150 the spatial resolution=0.200×0.200×0.200mm, acquisition time/scan = 5mins 38s. After five baseline scans, 30 μL of 25mM GadoSpin-P (Miltenyl Biotech GmBH, Germany) dissolved in sterile 0.9% NaCl was infused at a rate of 1.5 μL/min for 20min into

CSF through the cisterna magna catheter using an infusion pump. Post-contrast T1-weighted scans were acquired repetitively for ~180 min.

MRI data analysis

Brain morphometry: The 3D- proton density (PD) weighted images were corrected for intensity inhomogeneity caused by use of RF surface coil using the N4 bias field correction algorithm[52], and then segmented into grey matter (GM), white matter (WM) and CSF brain compartments to calculate their respective brain parenchymal (GM+WM) and CSF volumes. All the spatial segmentations were performed on SPM12 (http://www.fil.ion.ucl.ac.uk/spm) software package platform, using our custom-made tissue probability maps[53]. The GM, WM and CSF tissue probability maps generated by segmentation of individual rat brain were thresholded at 0.5, yielding GM, WM, and CSF binary masks in native space. We visually checked each mask compared with the corresponding PDW images and then manually edited the boundary of the CSF and tissue compartments to correct minor misclassification of tissue class mask using PMOD software (PMOD, version 3.908, PMOD Technologies LLC, Zürich, Switzerland).

Regional segmentation: Binary masks of regions of interests (ROIs) including the hippocampus, thalamus and the cerebellum were created by spatially normalizing ROIs included in the publicly available Waxholm rat brain atlas package[54] onto our custom-made CAA-SD template using the following processing steps: 1) Segmentation of the high-resolution Waxholm T2-weigted MRI image using our custom made rTg-DI/SD brain atlas template; 2) Normalization of the Waxholm brain atlas ROIs onto our custom-made template, using segmentation parameters derived from the previous step, thereby creating representative ROIs in our atlas; 3) Spatial warping of the representative ROIs from our custom-made rTg-DI/SD brain atlas into the native space of the individual rats using the segmentation parameters derived from rat brain segmentation mentioned in the brain morphometry section above. Each ROI was visually checked with PDW images and manually corrected for minor errors using PMOD (PMOD, version 3.908, PMOD Technologies LLC, Zürich, Switzerland).

Analysis of DCE-MRI data: The DCE-MRI data was corrected for head motion, followed by intensity normalization, smoothing, and then voxel-wise percent signal change to baseline was calculated using SPM12 (https://www.fil.ion.ucl.ac.uk/spm/) as previously described[7]. The ‘percent signal change from baseline images’ were then used for optimal mass transport (rOMT) analysis.

Whole brain DCE-MRI analysis: Detailed descriptions of the mathematical theory and numerical algorithms for the rOMT methodology and Lagrangian analysis of the DCE-MRI data can be found in Supplementary Methods. Briefly, from each rat’s whole brain DCE-MRI data series the rOMT analysis produced the following major outputs: 1) whole brain binary pathlines (representing the solute and fluid trajectories over ~2h), 2) voxel-wise whole brain speed maps (representing the local speed and spatial distribution of the pathline networks), 3) voxel-wise whole brain *Pe* map (representing the local Péclet number of the pathlines), and 4) whole brain velocity flux vectors representing the distance and direction of solute transport over ~2h. From the rOMT outputs, the total pathline volume, mean pathline speed and mean pathline Péclet number were extracted from the CSF and brain parenchymal compartments as well as from the hippocampus, and cerebellum (PMOD, version 3.908, PMOD Technologies LLC, Zürich, Switzerland) using the respective masks derived from the morphometric analysis. Speed map analysis via SPM analysis: Each 3D-proton density (PD) weighted image was corrected for signal intensity inhomogeneity caused by RF surface coil using the N4 bias field correction algorithm [82]. The bias field corrected 3D-PD weighted images were then segmented using our custom-made tissue probability maps[36] to generate deformation fields. These deformation fields of the individual rat brain were used to spatially normalize their corresponding speed maps. The isotropic 0.4 mm full width half maximum Gaussian smoothing kernel was then applied on the normalized speed maps. The voxel-wise statistical analysis between WT and rTg-DI rats was performed on the smoothened speed maps, for each age cohort (3M, 6M, and 12M), using and independent two-sample t-test in the framework of general linear modeling with the total intracranial volume (TIV) as a covariate. All the spatial segmentation, normalization, and statistical analysis were performed on SPM12 (http://www.fil.ion.ucl.ac.uk/spm) software package platform.

Neck DCE-MRI analysis: The DCE-MRI data acquired on the neck underwent several processing steps using PMOD (PMOD, version 3.908, PMOD Technologies LLC, Zürich, Switzerland). Firstly, the time series of post-contrast T1-weighted images were summed and used as an anatomical template to identify and manually outline volume of interests (VOI) by two anatomical experts (HB and SK). The VOIs included the 1) cervical lymph nodes (parotid lymph nodes, submandibular lymph nodes, and the deep cervical lymph nodes (dcLN)); 2) large arteries (common carotid artery, internal carotid artery and external carotid artery); 3) brain and spine; 4) CSF compartment of spine and brain, and 5) masks that included the right or the left dcLN and their corresponding carotid arteries. Second, time signal curves (TSC) were imported into PMOD and viewed in cine mode to allow for visualization of signal changes in areas of interest including large neck vasculature, cervical lymph nodes and other structures in proximity to the dcLN. The cine mode viewing of the DCE-MRI data also allowed for evaluation of pulsation artefacts from the carotid arteries interfering with signal changes in the dcLN located. DCE-MRI data with severe carotid blood flow artefacts overlapping with the dcLN signals were excluded from analysis. Thirdly, the CSF VOI was used to normalize the TSC to the signal input of the CSF compartment wherein the paramagnetic tracer (GadoSpin-P) is directly delivered as a normalization factor and used to calculate the normalized TSC. Fourthly, time signal curves (TSC) of each of the cervical lymph nodes were extracted from the normalized DCE-MRI. The normalized TSC underwent noise cancellation via a 2-time-step moving average analysis using XLSTAT (XLSTAT 2021.1.1, Addinsoft (2021). XLSTAT statistical and data analysis solution. New York, USA). The time-to-peak was extracted from the smoothed normalized TSC of the dcLN. All processing steps were carried out in MATLAB (R2021a) signal analyzer toolbox and functions. Finally, the masks of the right and left dcLN including carotid arteries were used for rOMT velocity flux vector analysis to define stream directional patterns in relation to the dcLN.

Immunohistochemistry, imaging, and quantification

Paraffin-fixed rat brain sections were cut in the sagittal plane at 10 μm thickness using a microtome (Leica, Buffalo Grove, IL), placed on Colorfrost plus microscope slides (Fisher, Pittsburgh, PA) and then rehydrated by immersing in xylene with decreasing concentrations of ethanol. Antigen retrieval was performed by incubation with proteinase K (0.2 mg/ml) for 5 min at 22° C. The treated tissue sections were then blocked in Superblock blocking buffer (cat. #37518, ThermoFisher, Bedford, MA) containing 0.3% Triton X-100 at room temperature for 30 min and incubated with individual primary antibodies at the following dilutions overnight: rabbit polyclonal antibody to collagen IV to detect cerebral blood vessels (1:250, SD2365885, Invitrogen, Carlsbad, CA), goat polyclonal antibody to glial fibrillary acidic protein (GFAP, 1:250, ab53554, Abcam, Cambridge, MA) to detect astrocytes, goat antibody to ionized calcium-binding adapter molecule 1 (Iba-1, 1:250, NB100–1028, Novus Biologicals, Centennial, CO) to detect microglia or rabbit polyclonal antibody to AQP4 (1:250, Novus Biologicals). Primary antibodies were detected with Alexa Fluorescent 594- or 488-conjugated secondary antibodies (1:1000). Deposited fibrillar amyloid was detected with Amylo-Glo (TR-300-AG, Biosensis Inc., Thebarton, South Australia), as described by the manufacturer. Images of Aβ labeled rat brain sections were captured on a KEYENCE BZ-X710 fluorescence microscope (Keyence, Itasca, IL).

Images for aquaporin-4 analysis were captured using an Axio Imager Z.2 multi-channel scanning fluorescence microscope equipped with a 20X/0.8 Plan-Apochromat objective (Carl Zeiss), a high-resolution ORCA-Fusion Digital CMOS camera (Hamamatsu Photonics), sensitive to a broad-spectrum of emission wavelengths, an X-Cite XYLIS broad-spectrum LED excitation source (Excelitas Technologies). Image tiles were individually captured at 0.32 μm/pixel spatial resolution and stitched into whole brain images using the ZEN Blue 2.1 image acquisition software (Carl Zeiss). The pseudo-colored stitched images were then exported to Photoshop (Adobe, 2020) and overlaid as individual layers to create whole brain multi-colored merged composites. For quantitative analysis in Fiji, individual ROIs were extracted and exported as TIFF files.

Aquaporin 4 (AQP4) polarization analysis: Quantification of AQP4 polarization was done in the ventral hippocampus using ImageJ software (Image J 1.52i) as previously described[7]. Briefly, the AQP4 digitized images were imported into ImageJ, scaled, and converted to optical density images. In order to process the samples in an unbiassed manner a grid (150 numbered boxes) was overlaid over the ventral hippocampus (each box area = 228 × 228 pixels). 15 boxes from hippocampal were randomly selected for a total of ~20 capillaries for WT rats and the same number of vessels in rTg-DI rats. Representative line segments (100 μm for capillaries) were used to extract immuno-intensity across the micro-vessels selected in each grid-box. The polarization index for each vessel was calculated from the optical density profiles of the AQP4 immunohistochemistry as the peak optical density/average baseline level as described in Koundal et al.,[7].

Data availability statement.—Statistical source data files depicting the quantification values mentioned in the text or plotted in graphs shown in Figs. 1, 2 and Extended Data Figs. 3, 5 and 6 are available in the online version of this paper. The rOMT processed speed maps and Péclet maps datasets generated from WT and rTg-DI and analyzed in the current study are available at https://zenodo.org/record/5809664#.Yczwyy2ZNBw.

Code availability: The rOMT code used for analysis of the DCE-MRI data is available https://zenodo.org/record/5809635#.YczwqS2ZNBw. Custom codes used for pre-processing of the DCE-MRI data sets for glymphatic analysis are available at https://zenodo.org/record/5809482#.YczwgC2ZNBw

Statistical analysis

Neither *a priori* nor a post hoc power analysis was conducted to formally determine or justify sample size due to the unknown effect size of the impact of evolving CAA pathology of the different age cohorts when planning the current study. Sample sizes were chosen on the basis of similar experiments previously published[7,23,38,55]. No randomization was performed. Two-way ANOVA models with independent variables including strain (rTg-DI vs WT rats), time (age: 3, 6, 12M) and the time x strain interaction were fit to compare the mean differences of different outcomes between rTg-DI and WT rats, between different time points (e.g., 3 vs 6M, 3 vs 12M, 6 vs 12M) within each strain of rats. No animals from the three different age cohorts of the WT and rTg-DI rats were excluded from the analysis. Note when comparing the CSF *v-flux* (or *speed*) and tissue *v-flux* (or *speed*) outcomes, the corresponding compartment volume was included as an extra independent variable in the ANOVA model. After all the modellings, the least square (marginal) mean difference (and 95% CI) of the outcomes was calculated as the effect size estimate, which would be informative in the design of a future study in which the sample size needs to be directly calculated based on a target statistical power (e.g., 80%) and significance level (e.g., 0.05) to detect a prespecified effect size. Comparison of ‘time-to-peak’ of the signal derived from the dcLN across WT and rTg-DI rats was performed using a Welch unequal variances two sample t-test (two-sided). Comparison of the capillary AQP4 polarization index for each age group (e.g., 3 vs 3M, 6 vs 6M) between WT and rTg-DI rats was done using a two-tailed Mann-Whitney U test. Experimenters were blinded to the identity of experimental groups from the time of euthanasia until the end of data collection and analysis for all the independent experiments. All the analyses were performed using IBM SPSS Statistics, Version 26. A p-value of less than 0.05 was chosen to indicate statistical significance and no adjustment of multiple testing was considered.

Extended Data

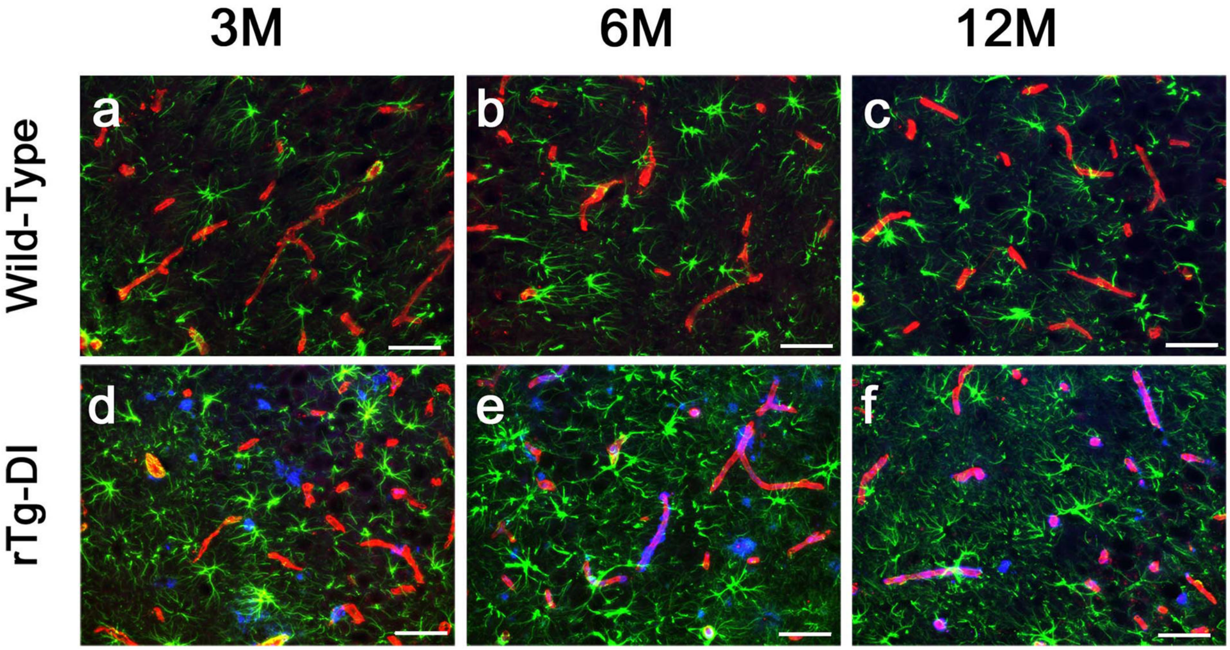

Extended Data Fig. 1. Progressive accumulation of microvascular amyloid and astrocytes in rTg-DI rats.

Brain sections from ventral hippocampus from **(a)** 3months (M), **(b)** 6M and **(c)** 12M wild-type rats and age-matched rTg-DI rats (**d-f**). The brain sections were labeled with Amylo-Glo to detect fibrillar amyloid (blue), rabbit polyclonal antibody to detect cerebral microvessels (red), and goat polyclonal antibody to GFAP to identify astrocytes (green). Scale bars = 50 μm. Note that an increased number of perivascular astrocytes is evident in rTg-DI rats as early as 3M. This experiment was independently repeated twice with similar results.

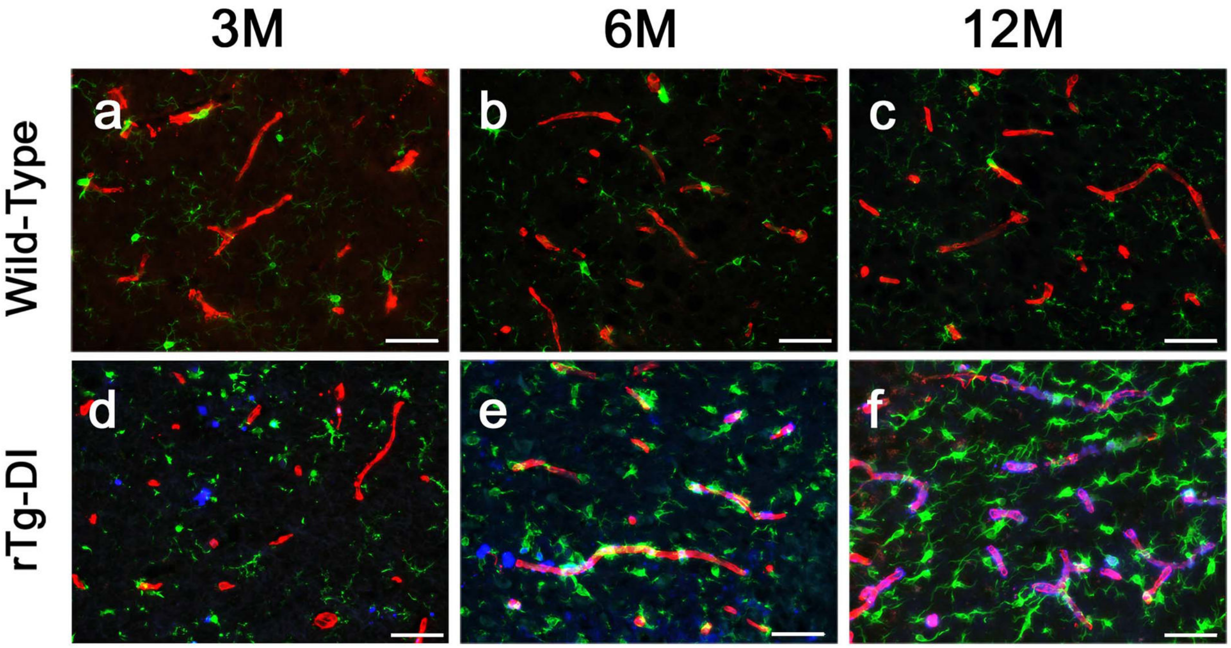

Extended Data Fig. 2. Increased perivascular microglia in rTg-DI rats

Brain sections from ventral hippocampus of **(a)** 3-month (M), **(b)** 6M and **(c)** 12 wild-type rats and age-matched rTg-DI rats (**d-f**). The brain sections were labeled with Amylo-Glo to detect fibrillar amyloid (blue), rabbit polyclonal antibody to detect cerebral microvessels (red), and goat polyclonal antibody to Iba-1 to identify microglia (green). Scale bars = 50 µm. Note that increased number of microglia cells are evident in rTg-DI rats as early as 3M. This experiment was independently repeated twice with similar results.

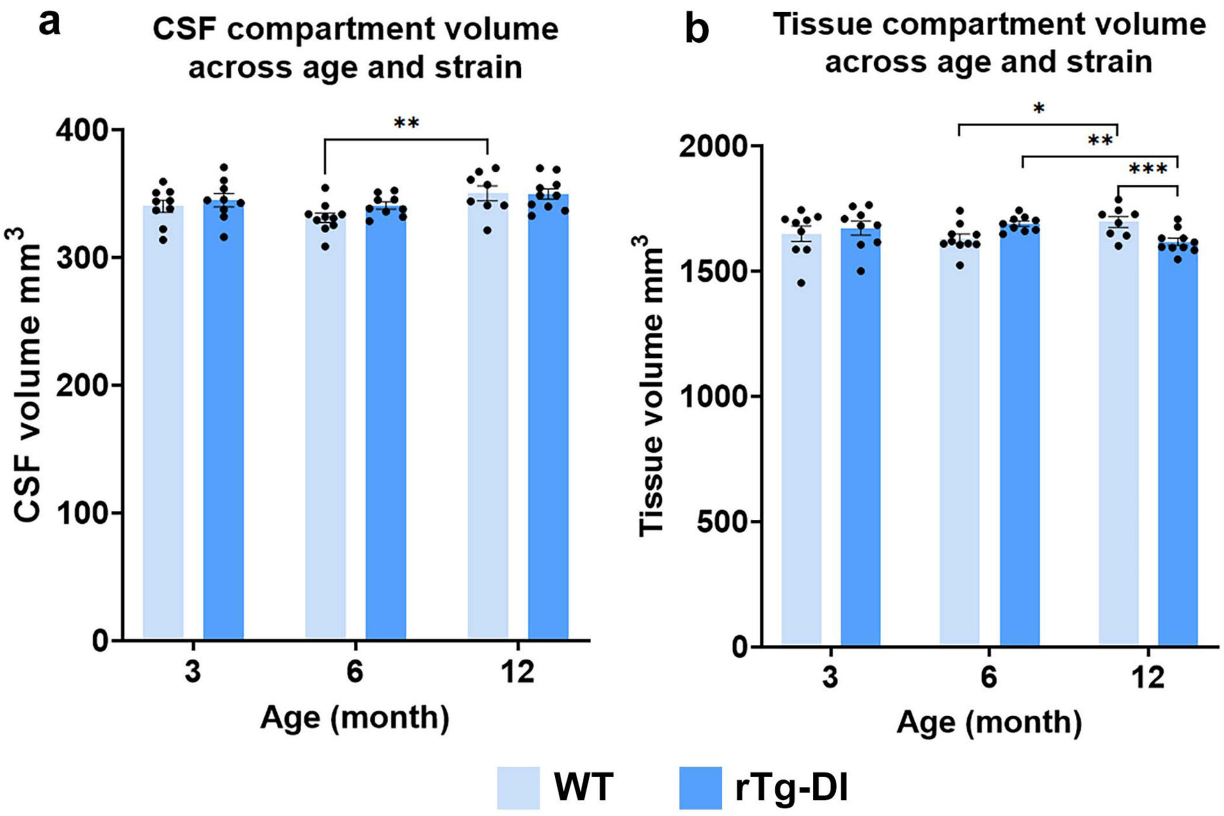

Extended Data Fig. 3. CSF and tissue volume changes across age and strain.

a Graph with quantification of CSF compartment volumes of the 3-month, (M) 6M and 12M WT (light blue bars) cohort and corresponding rTg-DI rat cohorts (blue bars). Each dot above the bar represents the value obtained from one rat. Note: WT n = 9, 10, 8 at 3,6 and 12 months; rTg-DI n = 9, 9, 10 at 3, 6, and 12 months, respectively from 3 independent experiments. Data are mean ± SEM. Statistical analysis with two-way ANOVA with independent variables including strain (rTg-DI vs WT rats), time (age: 3, 6, 12M) and the time × strain interaction were fit to compare the mean differences of different outcomes between rTg-DI and WT rats, between different time points within each strain of rats. A p-value of less than 0.05 was chosen to indicate statistical significance and no adjustment of multiple testing was considered. ******p-value = 0.004. **b** Graph with quantification tissue compartment volumes of the 3M 6M and 12M WT (light blue bars) and rTg-DI rat (blue bars) cohorts. Each dot above the bar represents the value obtained from one rat. Note: WT n = 9, 10, 8 at 3,6 and 12 months; rTg-DI n = 9, 9, 10 at 3, 6, and 12 months, respectively from 3 independent experiments. Data are mean ± SEM. Statistical analysis same as in b. *p-value = 0.038, **p-value = 0.021, ***p-value = 0.015.

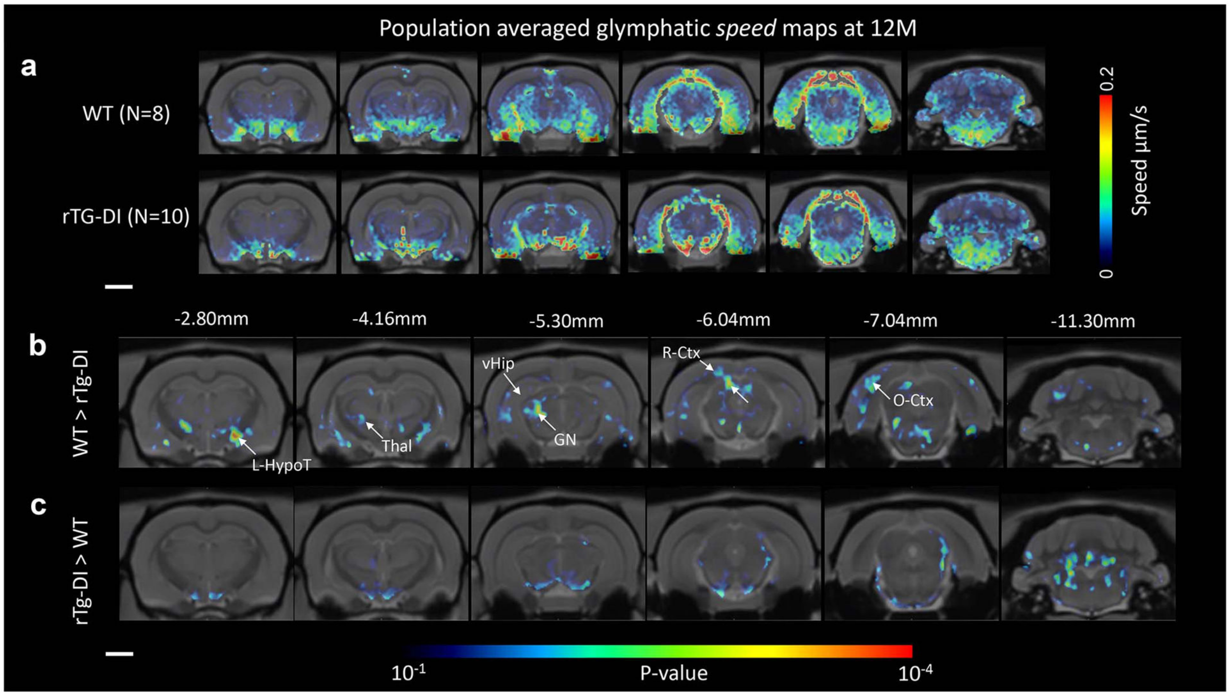

Extended Data Fig. 4. Significantly greater spatial distribution of glymphatic transport observed in WT compared to rTg-DI rats.

a Spatially normalized population averaged color coded speed maps of 12-month (M) old WT (N=8) and 12M rTg-DI (N=10) rats are shown overlaid onto population averaged proton density weighted anatomical MRI brain templates. **b** For the 12M WT (N=8) and 12M rTg-DI (N=10) cohorts, statistical parametric maps (color coded for p-values) were calculated at p-value < 0.05 and overlaid onto the MRI brain images to display anatomical areas with significant more speed in WT rats in comparison to rTg-DI rats or the reverse comparison. Note that the p-value map is uncorrected via the false-discovery rate procedure. Scale bars = 2mm. Anatomical levels of the axially displayed anatomical templates are given by their nearest Bregma distance. L-HypoT = left hypothalamus; Thal = thalamus; vHip = ventral hippocampus; GN = geniculate nucleus; R-Ctx = retro-splenial cortex; O-Ctx = Occipital cortex. Scale bar = 3 mm.

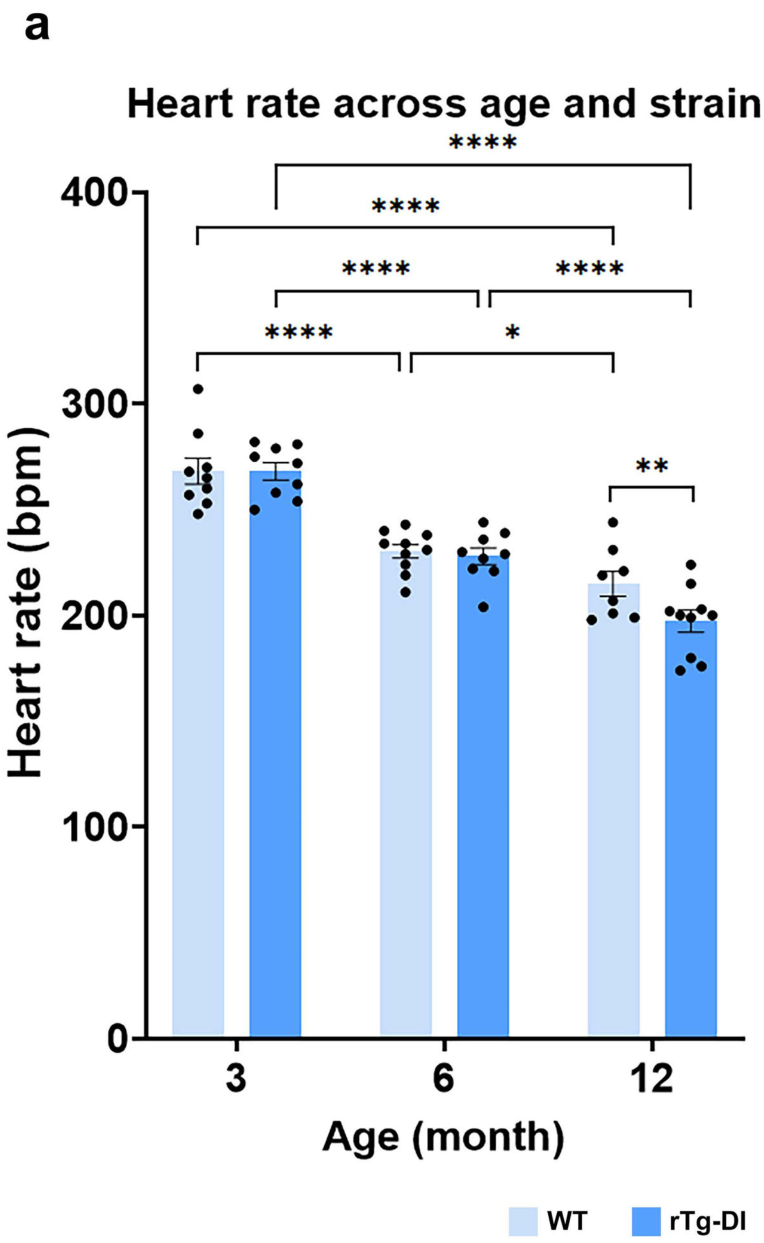

Extended Data Fig. 5. Heart rate changes across age and strains.

a Graph with quantification of the mean heart rate recorded of the anesthetized rats during MRI imaging from 3-month (M) 6M and 12M WT (light blue bars) and age-matched rTg-DI rats (blue bars). Each dot above the bar represents the mean heart rate recorded over the 2–3 h imaging period from one rat. Data are mean ± SEM. Note: WT n = 9, 10, 8 animals examined at 3,6 and 12 M, respectively, as independent experiments; rTg-DI n = 9, 9, 10 animals examined at 3,6 and 12 M, respectively, as independent experiments. Statistical analysis with two-way ANOVA with independent variables including strain (rTg-DI vs WT rats), time (age: 3, 6, 12M) and the time × strain interaction were fit to compare the mean differences of different outcomes between rTg-DI and WT rats, between different time points within each strain of rats. A p-value of less than 0.05 was chosen to indicate statistical significance and no adjustment of multiple testing was considered. *****p-value = 0.030, **p-value = 0.013, ****p-value < 0.0001.

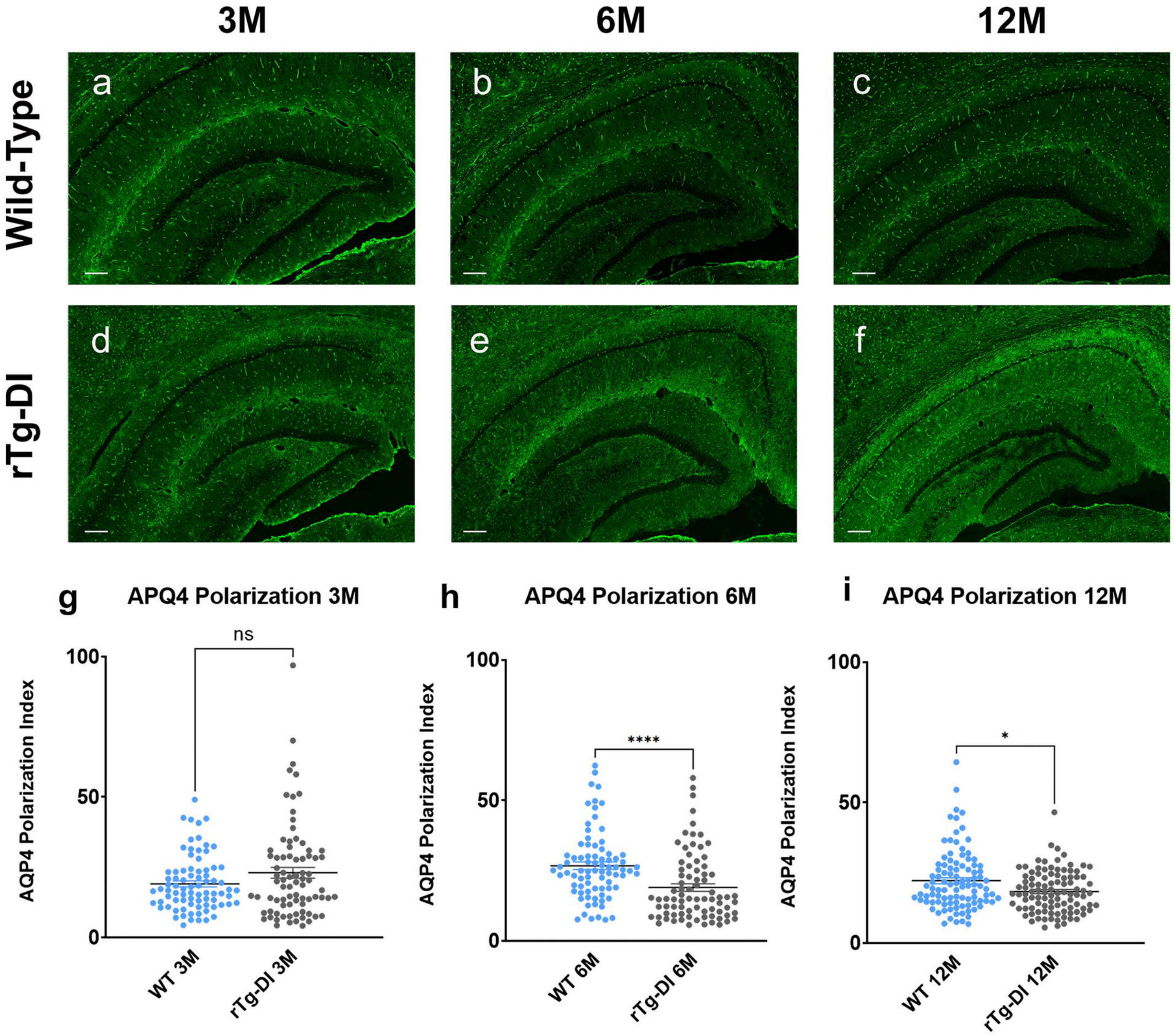

Extended Data Fig. 6. Perivascular AQP4 polarization of capillaries is impaired with evolving CAA

Changes in APQ4 localization was evaluated in WT and CAA rats by immunofluorescence. **a-c**: Representative slices at the level of the ventral hippocampus from 3M **(a)**, 6M **(b)** and 12M **(c)** WT rats showing strong perivascular AQP4 expression and localization across all age cohorts. **d-f** Corresponding brain slices at the level from age-matched rTg-DI rats demonstrating that the localization of perivascular AQP4 changes with evolving CAA pathology and is down-regulated in relation to the vasculature resulting in higher tissue ‘background’ AQP4 expression in 6M **(e)** and 12M **(f)** rTg-DI rats in comparison to 3M rTg-DI rats (D). Scale bar = 500 μ **g-i**: Graphs of quantification of AQP4 expression in perivascular domains surrounding capillaries in WT and rTg-DI rats. At 3M there are no differences in perivascular AQP4 expression across the strains **(g)**, however, at 6M and 12M the polarization index is decreased in rTg-DI compared to WT inferring more dispersed expression away from the capillary (**h, i**). Each dot represents the polarization from one capillary in the ventral hippocampus, with n=20 capillaries/rat and n=4 for 3M and 6M groups and 20capillaries/rat and n=5 for the 12M group from three independent experiments. Horizontal bars indicate mean ± SEM.; two-tailed Mann-Whitney U test. *p-value < 0.05, ****p-value < 0.0001.

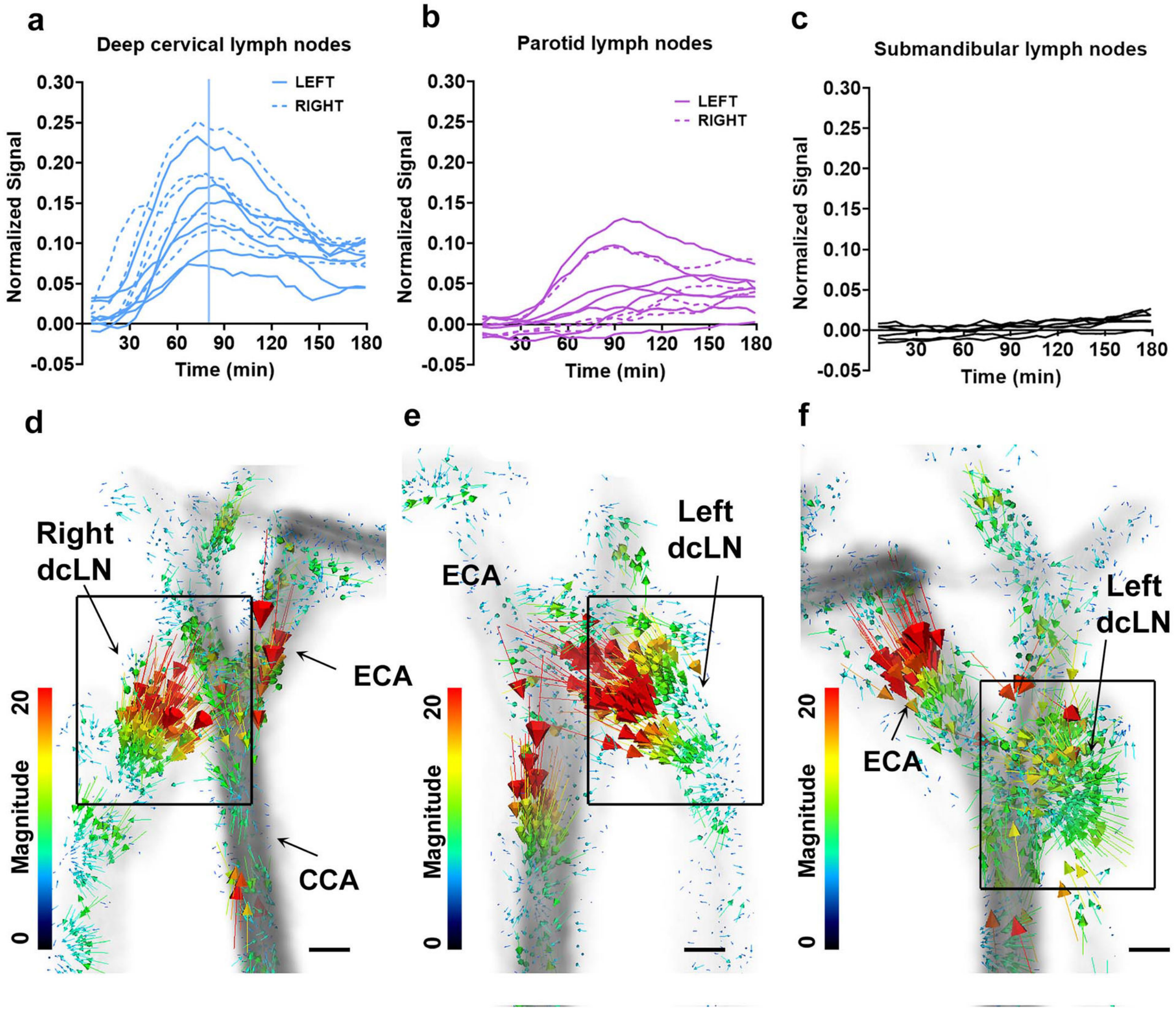

Extended Data Fig. 7. Drainage from CNS to cervical lymph nodes in normal SD rats.

a Graphs of time signal changes in individual right-sided (dashed blue lines) and left-sided (blue lines) deep cervical lymph nodes (dcLN) derived from independent experiments of n=6 normal Sprague Dawley (SD) rats. dcLN data from one rat was excluded to excessive vascular motion artefacts. Blue line indicates the mean peak time. **b** Corresponding graphs of time signal changes in individual right-sided (dashed magenta lines) and left-sided (magenta lines) parotid lymph nodes from the same cohort of normal SD rats. **c** Corresponding graphs of the time signal changes observed in the submandibular cervical lymph nodes (average of 2–3 nodes/rat) from the same cohort of normal SD rats. **d-f**: Velocity flux vectors – color coded for magnitude – from three different SD rats overlaid onto anatomical masks of the carotid arteries and dcLN showing the direction of solute drainage along the external carotid artery and within the carotid bifurcation towards the dcLN (black boxes). Scale bars = 1 mm.

Supplementary Material

Refer to Web version on PubMed Central for supplementary material.

Acknowledgements

The authors thank Peter Brown of MRRC (Magnetic Resonance Research Center) at Yale University for coil development and support. We also thank Lucy Zhao for editing our manuscript.

Funding:

This work was supported by a grant from the National Institutes of Health/National Institute on Aging, AG053991 (HB, AT and WVN).

Competing interest

H.B. received research support from PureTech. J.K. is a member of the scientific advisory group for PureTech. J.K. The remaining authors declare no competing interests.

References

1. Pfeifer LA, White LR, Ross GW, Petrovitch H & Launer LJ Cerebral amyloid angiopathy and cognitive function: the HAAS autopsy study. Neurology 58, 1629–1634, doi:10.1212/wnl.58.11.1629 (2002). [PubMed: 12058090]
2. Matthews FE et al. Epidemiological pathology of dementia: attributable-risks at death in the Medical Research Council Cognitive Function and Ageing Study. PLoS Med 6, e1000180, doi:10.1371/journal.pmed.1000180 (2009). [PubMed: 19901977]
3. Banerjee G et al. Cognitive Impairment Before Intracerebral Hemorrhage Is Associated With Cerebral Amyloid Angiopathy. Stroke 49, 40–45, doi:10.1161/STROKEAHA.117.019409 (2018). [PubMed: 29247143]
4. Thal DR et al. Two types of sporadic cerebral amyloid angiopathy. J Neuropathol Exp Neurol 61, 282–293 (2002). [PubMed: 11895043]
5. Attems J, Jellinger K, Thal DR & Van Nostrand W Review: sporadic cerebral amyloid angiopathy. Neuropathol Appl Neurobiol 37, 75–93, doi:10.1111/j.1365-2990.2010.01137.x (2011). [PubMed: 20946241]
6. Elkin R et al. GlymphVIS: Visualizing glymphatic transport pathways using regularized optimal transport. Med Image Comput Comput Assist Interv 11070, 844–852, doi:10.1007/978-3-030-00928-1_95 (2018). [PubMed: 30906935]
7. Koundal S et al. Optimal Mass Transport with Lagrangian Workflow Reveals Advective and Diffusion Driven Solute Transport in the Glymphatic System. Sci Rep 10, 1990, doi:10.1038/s41598-020-59045-9 (2020). [PubMed: 32029859]
8. Rustenhoven J et al. Functional characterization of the dural sinuses as a neuroimmune interface. Cell 184, 1000–1016 e1027, doi:10.1016/j.cell.2020.12.040 (2021). [PubMed: 33508229]
9. Alves de Lima K, Rustenhoven J & Kipnis J Meningeal Immunity and Its Function in Maintenance of the Central Nervous System in Health and Disease. Annu Rev Immunol 38, 597–620, doi:10.1146/annurev-immunol-102319-103410 (2020). [PubMed: 32340575]
10. Kress BT et al. Impairment of paravascular clearance pathways in the aging brain. Ann Neurol 76, 845–861, doi:10.1002/ana.24271 (2014). [PubMed: 25204284]
11. Ma Q, Ineichen BV, Detmar M & Proulx ST Outflow of cerebrospinal fluid is predominantly through lymphatic vessels and is reduced in aged mice. Nat Commun 8, 1434, doi:10.1038/s41467-017-01484-6 (2017). [PubMed: 29127332]

12. Da Mesquita S et al. Functional aspects of meningeal lymphatics in ageing and Alzheimer's disease. Nature 560, 185–191, doi:10.1038/s41586-018-0368-8 (2018). [PubMed: 30046111]
13. Peng W et al. Suppression of glymphatic fluid transport in a mouse model of Alzheimer's disease. Neurobiology of disease 93, 215–225, doi:10.1016/j.nbd.2016.05.015 (2016). [PubMed: 27234656]
14. Ding XB et al. Impaired meningeal lymphatic drainage in patients with idiopathic Parkinson's disease. Nat Med, doi:10.1038/s41591-020-01198-1 (2021).
15. Biffi A & Greenberg SM Cerebral amyloid angiopathy: a systematic review. J Clin Neurol 7, 1–9, doi:10.3988/jcn.2011.7.1.1 (2011). [PubMed: 21519520]
16. Wermer MJH & Greenberg SM The growing clinical spectrum of cerebral amyloid angiopathy. Curr Opin Neurol 31, 28–35, doi:10.1097/WCO.0000000000000510 (2018). [PubMed: 29120920]
17. Greenberg SM Cerebral amyloid angiopathy: prospects for clinical diagnosis and treatment. Neurology 51, 690–694 (1998). [PubMed: 9748011]
18. Albargothy NJ et al. Convective influx/glymphatic system: tracers injected into the CSF enter and leave the brain along separate periarterial basement membrane pathways. Acta Neuropathol 136, 139–152, doi:10.1007/s00401-018-1862-7 (2018). [PubMed: 29754206]
19. Carare RO et al. Solutes, but not cells, drain from the brain parenchyma along basement membranes of capillaries and arteries: significance for cerebral amyloid angiopathy and neuroimmunology. Neuropathol Appl Neurobiol 34, 131–144, doi:10.1111/j.1365-2990.2007.00926.x (2008). [PubMed: 18208483]
20. Iliff JJ et al. A paravascular pathway facilitates CSF flow through the brain parenchyma and the clearance of interstitial solutes, including amyloid beta. Science translational medicine 4, 147ra111, doi:10.1126/scitranslmed.3003748 (2012).
21. Nedergaard M & Goldman SA Brain Drain. Sci Am 314, 44–49, doi:10.1038/scientificamerican0316-44 (2016).
22. Davis J et al. A Novel Transgenic Rat Model of Robust Cerebral Microvascular Amyloid with Prominent Vasculopathy. Am J Pathol 188, 2877–2889, doi:10.1016/j.ajpath.2018.07.030 (2018). [PubMed: 30446159]
23. Lee H et al. Diffuse white matter loss in a transgenic rat model of cerebral amyloid angiopathy. J Cereb Blood Flow Metab, 271678X20944226, doi:10.1177/0271678X20944226 (2020).
24. Zhu X, Hatfield J, Sullivan JK, Xu F & Van Nostrand WE Robust neuroinflammation and perivascular pathology in rTg-DI rats, a novel model of microvascular cerebral amyloid angiopathy. J Neuroinflammation 17, 78, doi:10.1186/s12974-020-01755-y (2020). [PubMed: 32127016]
25. Iliff JJ et al. Cerebral arterial pulsation drives paravascular CSF-interstitial fluid exchange in the murine brain. The Journal of neuroscience: the official journal of the Society for Neuroscience 33, 18190–18199, doi:10.1523/JNEUROSCI.1592-13.2013 (2013). [PubMed: 24227727]
26. Rennels ML, Blaumanis OR & Grady PA Rapid solute transport throughout the brain via paravascular fluid pathways. Adv Neurol 52, 431–439 (1990). [PubMed: 2396537]
27. Zeppenfeld DM et al. Association of Perivascular Localization of Aquaporin-4 With Cognition and Alzheimer Disease in Aging Brains. JAMA Neurol 74, 91–99, doi:10.1001/jamaneurol.2016.4370 (2017). [PubMed: 27893874]
28. Iliff JJ et al. Brain-wide pathway for waste clearance captured by contrast-enhanced MRI. J Clin Invest 123, 1299–1309, doi:10.1172/JCI67677 (2013). [PubMed: 23434588]
29. Boyle PA et al. Cerebral amyloid angiopathy and cognitive outcomes in community-based older persons. Neurology 85, 1930–1936, doi:10.1212/WNL.0000000000002175 (2015). [PubMed: 26537052]
30. Esiri M et al. Cerebral amyloid angiopathy, subcortical white matter disease and dementia: literature review and study in OPTIMA. Brain Pathol 25, 51–62, doi:10.1111/bpa.12221 (2015). [PubMed: 25521177]
31. Hughes TM et al. Arterial stiffness and dementia pathology: Atherosclerosis Risk in Communities (ARIC)-PET Study. Neurology 90, e1248–e1256, doi:10.1212/WNL.0000000000005259 (2018). [PubMed: 29549223]

32. Riba-Llena I et al. Arterial Stiffness Is Associated With Basal Ganglia Enlarged Perivascular Spaces and Cerebral Small Vessel Disease Load. Stroke 49, 1279–1281, doi:10.1161/STROKEAHA.118.020163 (2018). [PubMed: 29669870]

33. Benveniste H & Nedergaard M Cerebral small vessel disease: A glymphopathy? Curr Opin Neurobiol 72, 15–21, doi:10.1016/j.conb.2021.07.006 (2021). [PubMed: 34407477]

34. Deane R et al. LRP/amyloid beta-peptide interaction mediates differential brain efflux of Abeta isoforms. Neuron 43, 333–344, doi:10.1016/j.neuron.2004.07.017 (2004). [PubMed: 15294142]

35. Tarasoff-Conway JM et al. Clearance systems in the brain-implications for Alzheimer disease. Nat Rev Neurol 11, 457–470, doi:10.1038/nrneurol.2015.119 (2015). [PubMed: 26195256]

36. Benveniste H et al. Anesthesia with Dexmedetomidine and Low-dose Isoflurane Increases Solute Transport via the Glymphatic Pathway in Rat Brain When Compared with High-dose Isoflurane. Anesthesiology 127, 976–988, doi:10.1097/Aln.0000000000001888 (2017). [PubMed: 28938276]

37. Hablitz LM et al. Increased glymphatic influx is correlated with high EEG delta power and low heart rate in mice under anesthesia. Sci Adv 5, eaav5447, doi:10.1126/sciadv.aav5447 (2019). [PubMed: 30820460]

38. Lee H et al. The Effect of Body Posture on Brain Glymphatic Transport. The Journal of neuroscience: the official journal of the Society for Neuroscience 35, 11034–11044, doi:10.1523/JNEUROSCI.1625-15.2015 (2015). [PubMed: 26245965]

39. Hablitz LM et al. Circadian control of brain glymphatic and lymphatic fluid flow. Nat Commun 11, 4411, doi:10.1038/s41467-020-18115-2 (2020). [PubMed: 32879313]

40. Wang MX, Ray L, Tanaka KF, Iliff JJ & Heys J Varying perivascular astroglial endfoot dimensions along the vascular tree maintain perivascular-interstitial flux through the cortical mantle. Glia 69, 715–728, doi:10.1002/glia.23923 (2021). [PubMed: 33075175]

41. Szentistvanyi I, Patlak CS, Ellis RA & Cserr HF Drainage of interstitial fluid from different regions of rat brain. Am J Physiol 246, F835–844, doi:10.1152/ajprenal.1984.246.6.F835 (1984). [PubMed: 6742132]

42. Yeo KP et al. Efficient aortic lymphatic drainage is necessary for atherosclerosis regression induced by ezetimibe. Sci Adv 6, doi:10.1126/sciadv.abc2697 (2020).

43. Yagmurlu K et al. Anatomical Features of the Deep Cervical Lymphatic System and Intrajugular Lymphatic Vessels in Humans. Brain Sci 10, doi:10.3390/brainsci10120953 (2020).

44. Kim MJ et al. Comparing the Organs and Vasculature of the Head and Neck in Five Murine Species. In Vivo 31, 861–871, doi:10.21873/invivo.11140 (2017). [PubMed: 28882952]

45. Szabo K The cranial venous system in the rat: anatomical pattern and ontogenetic development. II. Dorsal drainage. Ann Anat 177, 313–322, doi:10.1016/S0940-9602(11)80371-7 (1995). [PubMed: 7625604]

46. Weller RO, Subash M, Preston SD, Mazanti I & Carare RO Perivascular drainage of amyloid-beta peptides from the brain and its failure in cerebral amyloid angiopathy and Alzheimer’s disease. Brain Pathol 18, 253–266, doi:10.1111/j.1750-3639.2008.00133.x (2008). [PubMed: 18363936]

47. Aspelund A et al. A dural lymphatic vascular system that drains brain interstitial fluid and macromolecules. The Journal of experimental medicine 212, 991–999, doi:10.1084/jem.20142290 (2015). [PubMed: 26077718]

48. Louveau A et al. Structural and functional features of central nervous system lymphatic vessels. Nature 523, 337–341, doi:10.1038/nature14432 (2015). [PubMed: 26030524]

49. Antila S et al. Development and plasticity of meningeal lymphatic vessels. The Journal of experimental medicine 214, 3645–3667, doi:10.1084/jem.20170391 (2017). [PubMed: 29141865]

50. Benveniste H et al. Glymphatic Cerebrospinal Fluid and Solute Transport Quantified by MRI and PET Imaging. Neuroscience, doi:10.1016/j.neuroscience.2020.11.014 (2020).

51. Bolinger L, Prammer MG & Leigh JS A Multiple-Frequency Coil with a Highly Uniform B1 Field. Journal of Magnetic Resonance 81, 162–166, doi:Doi 10.1016/0022-2364(89)90274-6 (1989).

52. Tustison NJ et al. N4ITK: improved N3 bias correction. IEEE Trans Med Imaging 29, 1310–1320, doi:10.1109/TMI.2010.2046908 (2010). [PubMed: 20378467]

53. Koundal S et al. Brain Morphometry and Longitudinal Relaxation Time of Spontaneously Hypertensive Rats (SHRs) in Early and Intermediate Stages of Hypertension Investigated by

3D VFA-SPGR MRI. Neuroscience 404, 14–26, doi:10.1016/j.neuroscience.2019.01.030 (2019). [PubMed: 30690138]

54. Papp EA, Leergaard TB, Calabrese E, Johnson GA & Bjaalie JG Waxholm Space atlas of the Sprague Dawley rat brain. Neuroimage 97, 374–386, doi:10.1016/j.neuroimage.2014.04.001 (2014). [PubMed: 24726336]
55. Mortensen KN et al. Impaired Glymphatic Transport in Spontaneously Hypertensive Rats. The Journal of neuroscience: the official journal of the Society for Neuroscience 39, 6365–6377, doi:10.1523/JNEUROSCI.1974-18.2019 (2019). [PubMed: 31209176]

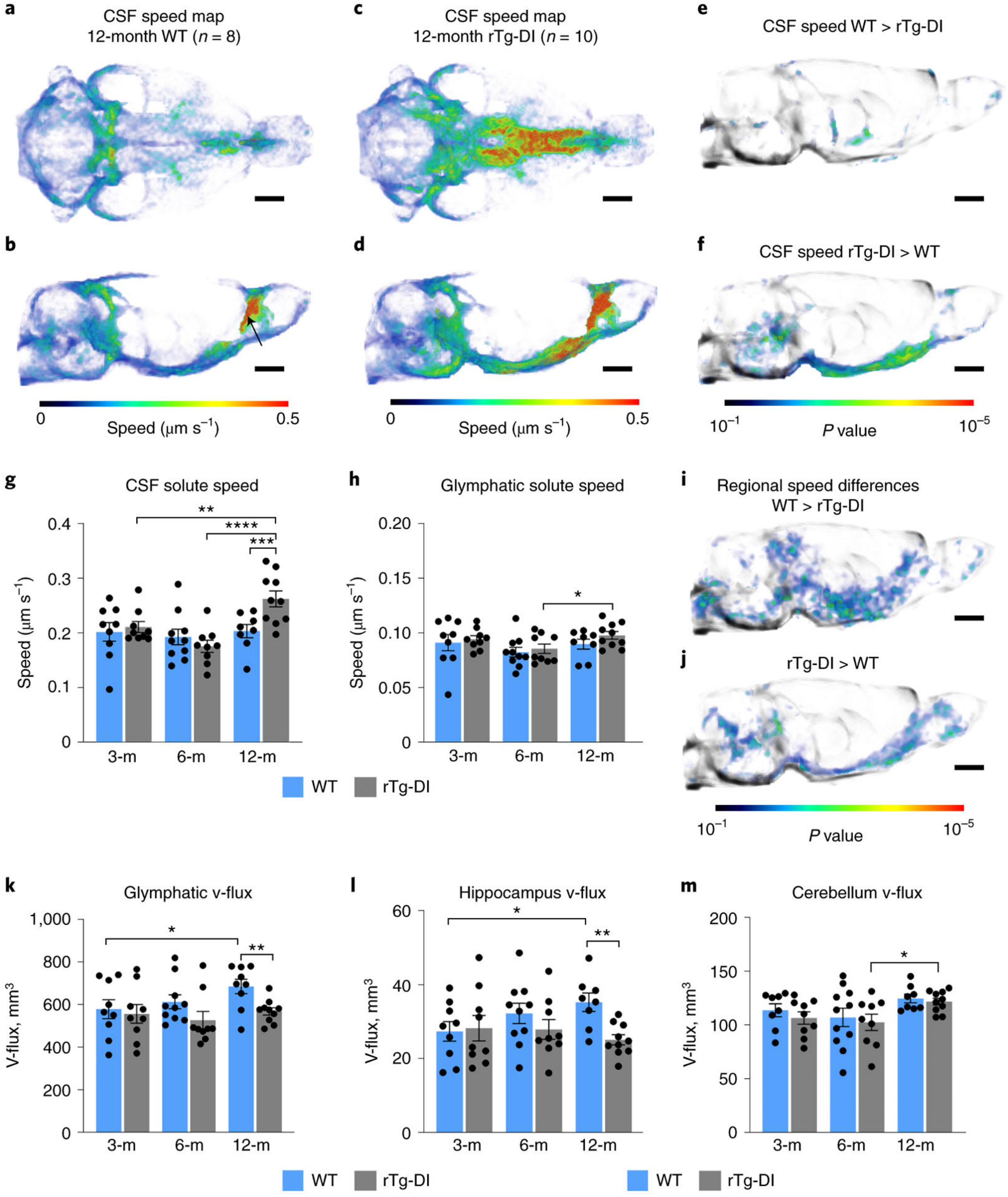

Fig. 1: CSF flow speed becomes hyperdynamic with severe CAA

a, b Spatially normalized population-averaged CSF speed maps of the 12M WT cohort (N=8) shown in two orthogonal plane views. Black arrow in **b** points to the olfactory fossa. **c, d** Corresponding CSF speed map of the 12M rTg-DI cohort (N=10) showing fast speed trajectories throughout the CSF compartment. Scale bars = 2mm. **e, f** Statistical parametric maps (color coded for p-values) overlaid onto a CSF binary map highlighting areas with differences in speed for two conditions: WT > rTg-DI (**e**) and rTg-DI > WT (**f**). Scale bars = 2mm. **g** Graph with quantification CSF *speed* of WT (blue bars) and rTg-DI rats (grey bars). Each dot above the bar represents values from one rat. Data are mean ± SEM, two-way ANOVA with CSF volume as a covariate factor. **p-value = 0.013, ***p = 0.003. ****p < 0.0001. **h** Graph with quantification of mean glymphatic solute speed from WT and rTg-DI rats. Data are mean ± SEM, two-way ANOVA with tissue volume as a covariate factor. *p-value = 0.044. **i, j** Statistical parametric maps (color coded for p-values) show tissue areas with differences in solute speed for two conditions: WT > rTg-DI (**i**) and rTg-DI > WT (**j**). **k** Graph with quantification of glymphatic (tissue) v-flux from WT and rTg-DI rats. Data are mean ± SEM, two-way ANOVA with tissue volume as a covariate factor. *p-value = 0.037, **p-value = 0.017. **l, m** Graphs of v-flux from the hippocampus and cerebellum of WT and rTg-DI rats. Data are mean ± SEM, two-way ANOVA. Hippocampus v-flux: *p-value = 0.045, **p-value = 0.009. Cerebellum v-flux: *p-value = 0.035. Note for **g, h** & **k-l**: WT n = 9, 10, 8 animals examined at 3,6 and 12 months, respectively, as independent experiments; rTg-DI n = 9, 9, 10 animals examined at 3,6 and 12 months, respectively, as independent experiments. A p-value of less than 0.05 was chosen to indicate statistical significance and no adjustment of multiple testing was considered.

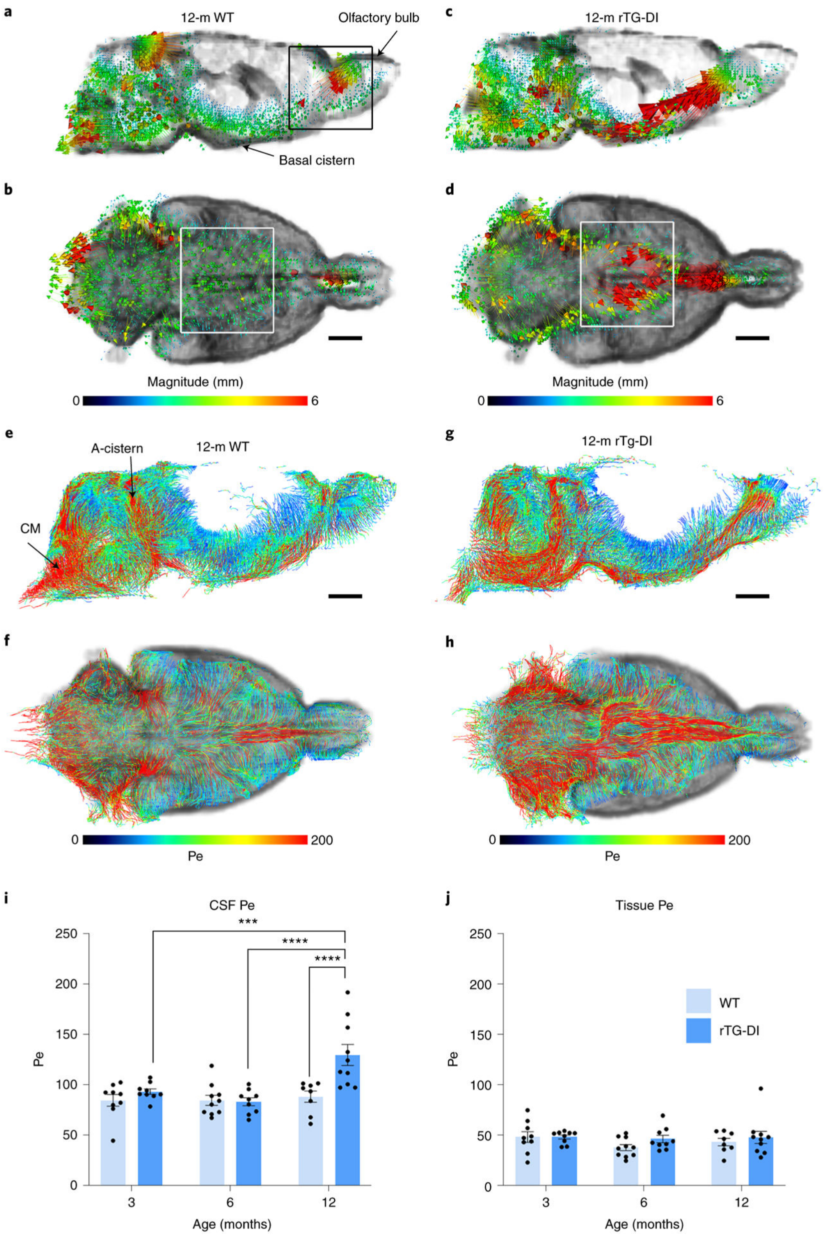

Fig. 2: CSF flow currents partly divert away from the glymphatic system in CAA type 1

a, b Representative examples of velocity flux vectors (color coded for magnitude) in two orthogonal planes from a 12M WT rat. The black box highlights the olfactory fossa. Scale bar = 3mm. **c, d** Corresponding velocity flux vectors from a 12M rTg-DI rat showing different magnitude and directional pattern on the skull base. Scale bar = 3mm. White boxes in **b** and **d** highlight the Circle of Willis area showing that vectors are directed towards the olfactory bulb. **e, f** Representative examples of pathlines endowed with color coded Péclet (*Pe*) values from 12M WT rat. The red and blue colors indicate advection-dominated diffusion-dominated regions, respectively. Note the advection-dominated areas dominate the CSF compartment. **g, h** Corresponding pathlines endowed with color coded *Pe* values from a 12M rTg-DI rat with end-stage CAA disease demonstrating strong advective current along the skull base. CM = cisterna magna; A-cistern = ambient cistern. Scale bars = 3mm. **i, j,** Graphs with quantification of CSF and tissue Péclet number of 3-month, (M) 6M and 12M WT (light blue bars) and rTg-DI rats (blue bars). Each dot above the bar represents the value obtained from one rat. Note: WT n = 9, 10, 8 at 3, 6 and 12 months, respectively; rTg-DI n = 9, 9, 10 at 3, 6, and 12 months, respectively from three independent experiments. Data are mean ± SEM. Statistical analysis with two-way ANOVA with independent variables including strain (rTg-DI vs WT rats), time (age: 3, 6, 12M) and the time x strain interaction were fit to compare the mean differences of different outcomes between rTg-DI and WT rats, between different time points within each strain of rats. A p-value of less than 0.05 was chosen to indicate statistical significance and no adjustment of multiple testing was considered. *******p-value < 0.001, ****p-value < 0.0001.

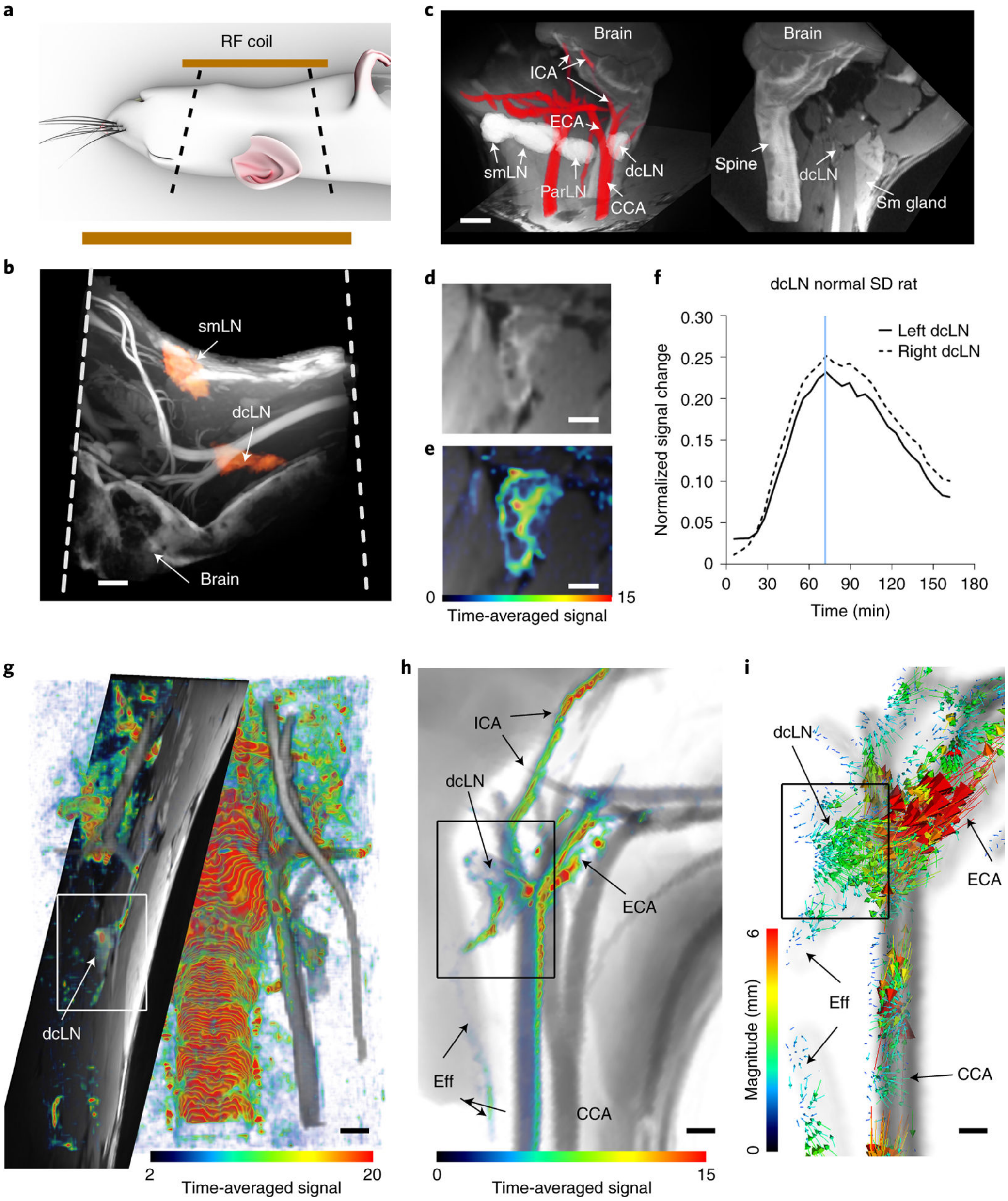

Fig. 3. Dynamic MRI for tracking cervical lymph node drainage from CNS in normal rats

a Illustration of the radiofrequency (RF) surface coil positioned above the neck of the rat. **b** The entire field-of-view captured in the neck region visualized as a 3D maximum intensity projection (MIP) image. The submandibular lymph nodes (smLN) and deep cervical lymph nodes (dcLN) are outlined (orange) to illustrate their locations in relation to brain, spine, and neck vasculature. **c** 3D MIPs show anatomical landmarks for locating the cervical lymph nodes in relation to the vasculature (red). Scale bar = 1mm. ICA=Internal carotid artery; ECA=external carotid artery, ParLN=Parotid lymph node. CCA=common carotid artery, sm Gland=submandibular gland. **d** MRI of dcLN from a normal rat acquired at a voxel resolution of 0.008 mm^3. **e** Corresponding solute drainage map of the dcLN. Drainage is represented by color-coded signal intensity normalized to the CSF signal and time-averaged over ~2hr. Scale bars = 2 mm. **f** Time signal curves of tracer uptake in the left- and right-dcLNs from a normal rat. Blue line indicates the time of peak signal. **g** Front view of a 3D signal map of the entire field-of-view of the neck area from a normal rat. The color-coded map represents the total signal, time averaged over the ~2hr from the time of CSF administration of GadoSpin. The large vessels are displayed as a grey-scale binary mask. High signal intensity areas represent GadoSpin predominantly in the CSF compartment. Anatomical map showing the location of the right dcLN positioned lateral to the carotid arteries. **h:** Distinct signal (drainage) streams along the neck arteries and dcLN on the right side from a normal rat. Streams along the external carotid artery (ECA) and at the CCA bifurcation appear to merge with the dcLN. The efferent lymphatic vessel (Eff) is also visible. **i:** Corresponding vector velocity flux vectors (color coded for magnitude) are shown overlaid on a mask of the arteries. High magnitude velocity flux vectors along the ECA pointing towards the dcLN are noted.

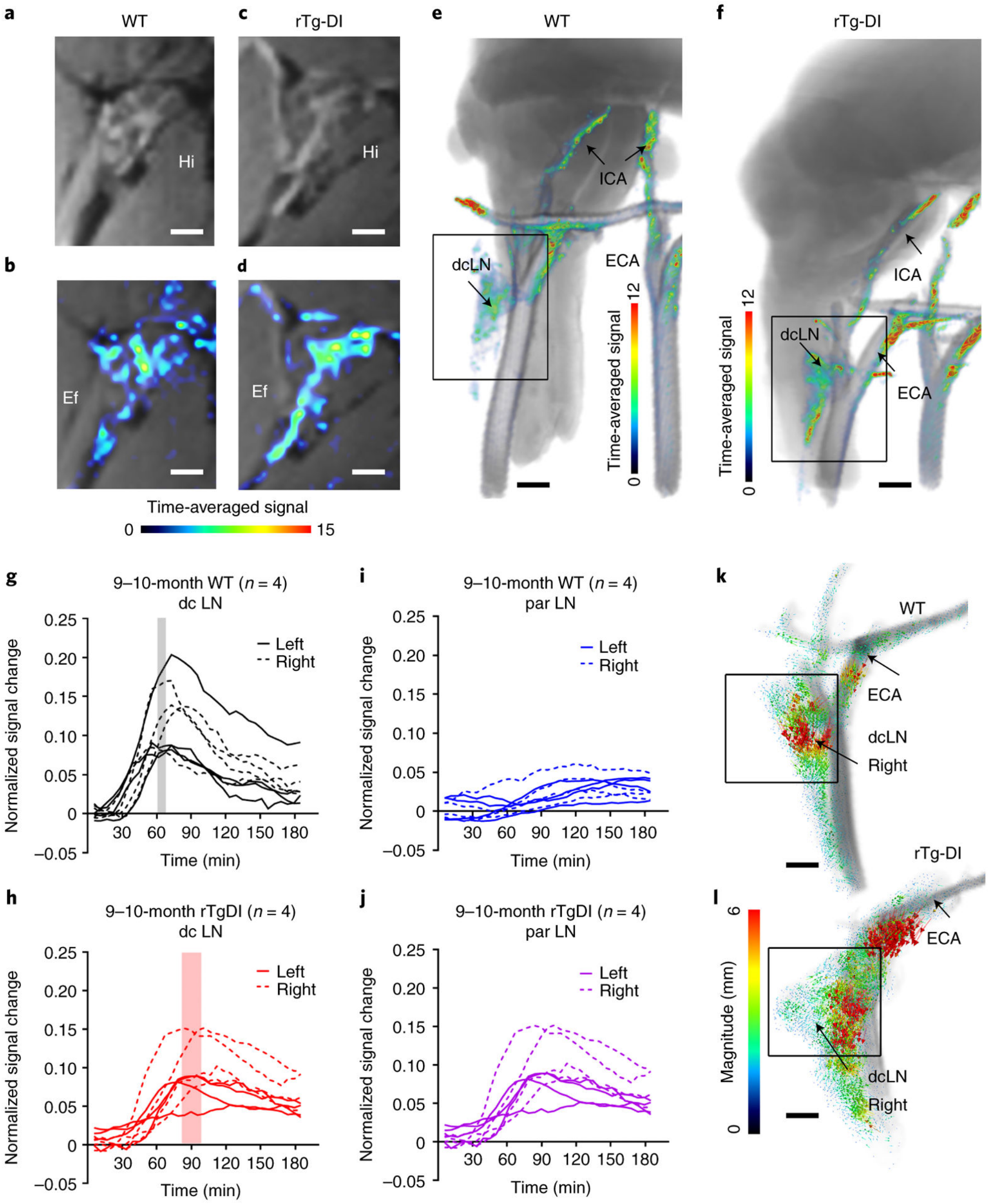

Fig. 4. Drainage to the cervical lymph nodes is sustained but time-delayed in rTg-DI rats

a Summed post-contrast anatomical MRI images of a deep cervical lymph node (dcLN) from a normal 9 month (M) old WT rat. **b** Corresponding dcLN drainage map represented by color-coded signal intensity time-averaged over ~2hrs and normalized to CSF signal intensity. Note higher signal intensity in the hilum (Hi) and efferent lymphatic vessel (Ef). **c, d** Corresponding images from a 9M rTg-DI rat showing similar draining pattern to the dcLN. a-d Scale bars = 2.0 mm. **e, f** 3D color-coded solute drainage maps showing discrete solute streams along the neck arteries and right dcLN from a 9M WT rat and a 9M rTg-DI rat. e, f Scale bars = 2mm. **g** Time signal curves (TSC) extracted from dcLNs derived from independent experiments of n=4 WT rats. Each line represents signal change in an individual right- or left-sided dcLNs and the rectangle represents the mean time-to-peak for solute drainage of all the dcLNs. **h** Corresponding TSC data extracted from dcLNs derived from independent experiments of n=4 rTg-DI rats. An independent, two-sided t-test revealed that the dcLN time-to-peak of rTg-DI rats was significantly longer than that of WT rats (left dcLN: p-value = 0.017; right dcLN: p-value = 0.007). **i, j** Corresponding TSC extracted from parotid lymph nodes from the same WT and rTg-DI rats. Each line represents an individual parotid lymph node. **k, l** Velocity flux vectors – color coded for magnitude – from one of the 9M WT and 9M rTg-DI rats overlaid on the corresponding anatomical template showing solute drainage along the external carotid artery (ECA) directed towards the dcLN (black box) in both rats. Scale bars = 1 mm.